© 2014

Michael Harten Koucky

ALL RIGHTS RESERVED

AXIAL RESPONSE OF HIGH-RESOLUTION MICROENDOSCOPY IN SCATTERING MEDIA, WITH AND WITHOUT STRUCTURED ILLUMINATION

By

MICHAEL HARTEN KOUCKY

A thesis submitted to the

Graduate School – New Brunswick

And

The Graduate School of Biomedical Sciences

Rutgers, The State University of New Jersey

in partial fulfillment of the requirements

for the degree of

Master of Science

Graduate Program in Biomedical Engineering

written under the direction of

Mark C. Pierce, PhD

and approved by

New Brunswick, New Jersey

January, 2014

ABSTRACT OF THE THESIS

Axial Response of High-Resolution Microendoscopy in Scattering Media, With and Without Structured Illumination

By MICHAEL HARTEN KOUCKY

Thesis Director:

Mark C. Pierce, PhD

High-resolution microendoscopy (HRME) uses epi-fluorescence imaging with a coherent fiber-optic bundle to enable *in vivo* examination of cellular morphology. While the HRME platform has recently gained popularity as a simple alternative to confocal endomicroscopy, the axial response of HRME in thick, scattering tissue has yet to be described quantitatively. This is important because when analyzing images collected by HRME, out-of-focus light may affect the accuracy of quantitative parameters such as nuclear-to-cytoplasm ratio, which has been proposed as a diagnostic indicator of dysplasia or cancer.

In the first part of this thesis, the imaging properties of the HRME system are investigated using phantoms simulating scattering tissue with fluorescently labeled nuclei. HRME images defocused (deep) objects with apparent diameters and intensity levels that are in agreement with a simple geometric model. Out-of-focus nuclei contribute a relatively low, uniform background level to images which neither leads to the erroneous appearance of large nuclei from deep layers, nor prevents accurate imaging of superficial nuclei with high contrast.

Proflavine has been used as a fluorescent contrast agent for HRME imaging, brightly labeling nuclei without staining the surrounding cytoplasm or organelles. If a non-specific fluorophore such as fluorescein is used, the removal of out-of-focus (OOF) light would be desirable. Optical sectioning is a property of some imaging systems, whereby OOF signal light is removed or rejected from the image. Optical sectioning is commonly associated with confocal microscopy and non-linear imaging methods such as multi-photon microscopy. In contrast, structured illumination (SI) is an imaging modality which is capable of providing optical sectioning without requiring raster scanning of a tightly focused laser beam. SI was integrated with the HRME platform and demonstrated to be an effective method of suppressing OOF signals, with comparable results to confocal. Theory, example images, programming considerations, and methods to minimize artifacts specific to SI are considered.

ACKNOWLEDGEMENTS

PUBLICATIONS & PRESENTATIONS

Portions of this thesis have been reported in the following publication and conference:

MH Koucky, MC Pierce, "Axial response of high-resolution microendoscopy in scattering media," *Biomed. Opt. Express* 4:10; 2247-2256 (2013).

MH Koucky, MC Pierce, " High-Resolution Microendoscopy and Structured Illumination for biopsy targeting," Poster presentation, CINJ Annual Retreat on Cancer Research, Piscataway, NJ, May 2013.

TABLE OF CONTENTS

Title Page i

Abstract ii

Acknowledgement iv

Table of Contents v

List of Illustrations vii

Chapter 1: Introduction 1

Chapter 2: Axial Response of High-Resolution Microendoscopy in Scattering Media 7

- 2.1: Introduction 7
- 2.2. Materials and methods 8
- 2.3. Results 15
- 2.4. Discussion & Conclusions 21

Chapter 3: Integration of Structured Illumination With HRME for Optical Sectioning 23

- 3.1. Introduction 23
- 3.2 Theoretical Basis of Structured Illumination Microscopy 24
- 3.3 Microscope System 28
- 3.4 Programming 30
- 3.5 System Validation 32
- 3.6 Image Artifacts 36

Chapter 4: Summary & Conclusions 45

References 47

LIST OF ILLUSTRATIONS

Fig. 1.1: Schematic illustrating (a) confocal microscope and (b) principle of optical sectioning due to pinhole. 3

Fig. 2.1: (a) Schematic diagram illustrating setup of the HRME / confocal optical rystem and (b) ray diagram of a geometric model for HRME. 9

Fig. 2.2: (a-h) HRME and confocal images and (i) apparent diameter and (j) intensity of 14.8 µm fluorescent beads as a function of defocus. 17

Fig. 2.3: (a-c) Apparent diameter and (d-f) intensity of 14.8 µm beads as a function of sub-surface depth in non-scattering, low-scattering, and high-scattering phantoms without a fiber-bundle. 18

Fig. 2.4: Images of 14.8 µm beads collected without (a-c) and with (d-f) a fiber-bundle. Apparent diameter (g-i) and intensity (j-l) of beads as a function of subsurface depth measured in non-scattering, low-scattering, and high-scattering phantoms, both with and without fiber-bundle. 19

Fig. 2.5: *In vivo* imaging of human oral mucosa following topical application of proflavine, using (a) HRME and (b) confocal microendoscope systems. 20

Fig. 3.1: Optically-sectioned SI image of a pollen grain, the same pollen grain in standard wide-field microscopy, and an example schematic of a SIM system [36]. 24

Fig. 3.2: (a) Three sinusoids in form of Eq. 3.1. with relative phase shifts ϕ = 0, 2π/3, and 4π/3 and (b) the same sinusoids recombined according to Eq. 3.3. 26

Fig. 3.3: (a) Example curve demonstrating image attenuation with axial defocus using SIM and (b) theoretical FWHM as a function of normalized grid spatial frequency. 27

Fig. 3.4: (a) Three square waves with relative phase shifts ϕ = 0, 2π/3, and 4π/3 and the same square waves recombined according to Eq. 3.3 28

Fig. 3.5: Schematic of the SI-HRME microscope 29

Fig. 3.6: Flow diagrams demonstrating various algorithms for SI programming 31

Fig. 3.7: (a) Intensity profile of a 15 µm thick object plane, (b) expected response of the SI system to an infinitely thin plane object at varying defocus, for 10 lp/mm and 40 lp/mm grids and experimental data from the 10 and 40 lp/mm SIM compared to theory. 33

Fig. 3.8: Standard epi-fluorescence images of lens paper (a) and fluorescent beads (d) compared to SI images at 10 lp/mm (b,e) and 40 lp/mm (c,f). 35

Fig. 3.9: Standard HRME images (a) and SI-HRME images of fluorescently labeled lens paper (b,c). 36

Fig. 3.10: Modeled effect of 5% phase shift error on the residual bar artifact when using the standard structured Illumination reconstruction algorithm. 37

Fig. 3.11: Example images of a plane mirror (a,b) and lens paper (c,d) showing residual bar artifact in SI imaging at 10 lp/mm (a,c) and 40 lp/mm (b,d). 39

Fig. 3.12: Cross-correlation of two line profiles extracted from images acquired for consecutive shifts of the 10 lp/mm grid. 40

Fig. 3.13: (a) Measured shift of the SI translation stage for fixed command shifts, at all locations along the stage's range of motion. (b,c) Measured shift per command step. (d) Predicted step size required for 336 and 100 step commands, using data to create a look-up table (LUT). 42

Fig. 3.14: Shift histograms for (a) a fixed number of (363) steps, (b) raw LUT, and (c-f) LUT after several rounds of "fixing" algorithm 44

Chapter 1: Introduction

Visual examination of tissue architecture at the cellular scale is required for clinical diagnosis and staging of many types of cancer. Histopathology is by far the most commonly employed technique for examination of cellular morphology, but requires invasive biopsy collection, processing, and reading by an expert pathologist. Screening and surveillance requires the collection of a biopsy from any suspicious site; in some diseases such as Barrett's esophagus, multiple biopsies are collected from the entire segment at risk (1). This approach can result in a large number of unnecessary biopsies being collected, or in truly abnormal tissue being missed. The ability to view tissues with cellular-scale resolution *in situ* would allow directed collection of biopsies, possibly improving diagnostic yield and reducing cost. Techniques such as confocal and multiphoton microscopy have shown feasibility of imaging with sub-cellular resolution in intact tissues, with fiber optic components providing access to sites within the body for microscopic imaging *in situ* (2).

Confocal microscopy is a point-scanning imaging method which uses a pinhole to reject out-of-focus (OOF) light. While confocal microscopy may, in principle, be performed in reflectance or fluorescence mode, in practice, use of fluorescent contrast agents to label specific tissue components is much more common. A schematic of fluorescence confocal microscopy is shown in Fig. 1.1 (a). A collimated laser beam is reflected by a dichroic beam-splitter to a pair of scanning mirrors, and then focused to a point. The pivoting action of the scanning mirrors results in raster (XY) scanning of the focused beam at the tissue. The incident laser light is absorbed by fluorophores within the focal cone and lower energy fluorescent emission is generated. A fraction of this emission signal is collected by the objective lens and passed back to the scanning mirrors, which has the effect of descanning the emitted signal light. The emission signal then passes through the dichroic mirror and is focused to a point. This point is conjugate (or "*confocal*") with the focal plane of the objective lens (hence the description *confocal microscopy*), and it is at this emission focus that a pinhole is placed. Any emission light from the sample which is not generated at the focal plane of the objective lens will not be focused at the confocal pinhole and will therefore be strongly attenuated by the pinhole. Fig. 1.1 (b) is a schematic demonstrating the effect of the confocal pinhole. Red lines, indicating the light cone originating from the focal plane, pass through the pinhole. Because the entire light cone is accepted by the pinhole, the signal intensity will not be attenuated. Green and blue lines, indicating light cones originating from above and below the focal plane, are mostly blocked by the pinhole meaning that their intensity will be strongly attenuated. The signal which passes the pinhole is then collected by a point detector (usually a photomultiplier tube or avalanche photodiode). The signal from the detector is digitized and can be used to construct an image by assigning a brightness (pixel value) to each location in the raster scan pattern.

Non-linear techniques such as two-photon microscopy also rely on point scanning of a laser excitation signal, using one or more high-powered pulsed lasers to generate various non-linear signals (e.g. multi-photon, second harmonic, coherent anti-Stokes Raman scattering). These non-linear signals are only generated at the point where the laser intensity is highest (i.e. at the beam focus). Because of this, no OOF signal is generated and no descanning or pinhole are required; all nonlinear emission inherently arises from the focal plane.

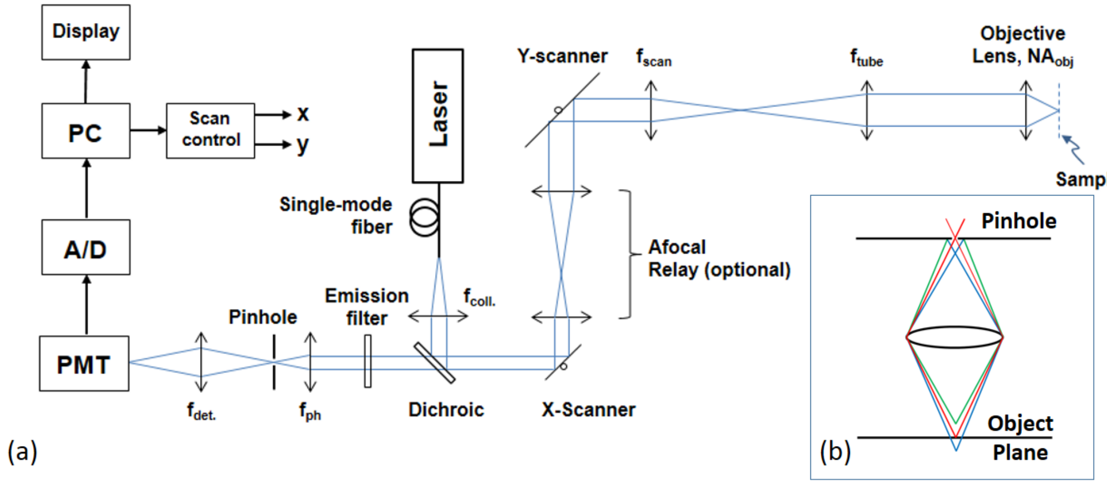
Display
PC
Scan control
x
y
A/D
PMT
Laser
Single-mode fiber
Y-scanner
f_{scan}
f_{tube}
Objective Lens, NA_{obj}
Sample
Afocal Relay (optional)
Emission filter
$f_{coll.}$
Pinhole
$f_{det.}$
f_{ph}
Dichroic
X-Scanner
(a)
Pinhole
Object Plane
(b)

Fig. 1.1: (a) Schematic of a typical confocal microscope (b) Schematic of the effect of the confocal pinhole, creating optical sectioning by preventing out-of-focus light (red and blue rays) from reaching the detector.

In order to access and image organs within the body using point-scanning confocal or nonlinear microscopy, fiber-optic components are commonly applied. Single-mode fiber delivery systems can have sub-millimeter diameters, but require a compact scanning mechanism at the distal tip (3-7). Alternatively, this miniaturization can be avoided by scanning the beam at the proximal end of a coherent fiber-optic bundle (8-10). Both single-mode fiber and bundle-based endomicroscopy systems can also incorporate miniature focusing optics at the distal tip, either in a fixed position (which defines the working distance to the image plane), or with an axial translation mechanism to obtain optical sections at specific depths within the imaging range.

Conventional microscopy has lateral and axial point spread function (PSF) (11, 12) given in Eq. 1.1 below:

$$I(r) \propto \left[\frac{2\,J_1\left(\frac{2\pi NA}{\lambda}r\right)}{\left(\frac{2\pi NA}{\lambda}r\right)}\right]^2 \qquad I(z) \propto \left[\frac{sin\left(\frac{\pi NA^2}{2\lambda}z\right)}{\left(\frac{\pi NA^2}{2\lambda}z\right)}\right]^2 \tag{1.1}$$

The axial PSF, however, does not apply to the imaging of a plane sample. In this case conventional microscopy will not experience any appreciable loss of intensity. In confocal microscopy, the PSF is given by multiplying the PSFs of the illumination and detection systems of the microscope. If the same optics are used for both and the excitation and emission wavelengths are relatively near one another, the lateral and axial PSFs can be approximated (11):

$$I(r) \propto \left[\frac{2\,J_1\left(\frac{2\pi NA}{\lambda}r\right)}{\left(\frac{2\pi NA}{\lambda}r\right)}\right]^2 \qquad I(z) \propto \left[\frac{sin\left(\frac{\pi NA^2}{\lambda}z\right)}{\left(\frac{\pi NA^2}{\lambda}z\right)}\right]^2 \tag{1.2}$$

Furthermore, the equations above apply to an infinitely small pinhole. In real imaging systems a finite pinhole is used. Increasing pinhole sizes have been shown to cause a widening of both the lateral and axial resolution (13). In the lateral case, the resolution quickly degenerates until it performs no better than conventional microscopy. The axial resolution also degrades with increasing pinhole size until it converges with conventional microscopy; however, the degradation in this case does not occur as quickly as with the lateral case. This allows the operator to control the section thickness by adjusting the diameter of the pinhole used.

Several studies have investigated the effects of integrating a fiber-optic imaging bundle (14-16). The effect of the fiber bundle on lateral resolution is relatively straightforward, due to the pixilation of the image by the fiber bundle, the resolution will be twice the center-to-center separation of the individual fibers. In the paper by Gmitro and Aziz which first introduced confocal microscopy through a fiber-optic imaging bundle in 1993 (14), the effect of the fiber bundle on axial response was investigated. This paper conclusively demonstrated that confocal microscopy retains its optical sectioning even when imaging through a fiber bundle as long as the projected size of the pinhole at the proximal fiber face is smaller than the size of an individual fiber. If the pinhole is larger than an individual fiber, the fiber then acts as a pinhole and the axial resolution will be degraded.

Additionally, it was demonstrated in 1997 by Juškaitis, Wilson, and Watson (17) that for defocus below a certain threshold, in their case ~2 µm, optical sectioning was independent of the pinhole diameter and the sectioning which occurred was due to the fiber behaving as a pinhole. Interestingly, in the case where no pinhole was used, the same axial response was observed until the ~2 µm threshold, then the response levels off at 60% of peak intensity. It was explained that for very small pinhole values, light from nearby fibers is blocked by the pinhole, but for larger pinhole values light from nearby fibers can pass through to the detector for greater defocus.

High-resolution microendoscopy (HRME) is a recently developed alternative to confocal or multiphoton imaging. It is also a fiber-optic imaging modality but is significantly simpler and cheaper to assemble than confocal or multiphoton modalities. However, this simplicity comes at the cost of optical sectioning; in principle the HRME should behave like a conventional epi-fluorescence microscope with no means to reject

OOF light. Nevertheless, other researchers have shown that HRME can generate high contrast images *in vivo* when used with highly specific fluorescent contrast agents (18-20). While these findings add to the appeal of HRME, they have raised questions concerning the actual degree to which HRME collects or blocks OOF light. In the first section of this thesis I quantify the effects of OOF light on HRME imaging using fluorescent beads in a phantom system, allowing for the first time a direct comparison of background rejection in HRME and confocal microendoscopy. In the second section I demonstrate how implementation of structured illumination in the HRME system can add optical sectioning to potentially enable its use with a broader range of fluorescent contrast agents.

Chapter 2: Axial Response of High-Resolution Microendoscopy in Scattering Media

2.1 Introduction

High-resolution microendoscopy (HRME) is a fiber-optic bundle based epi-fluorescence imaging modality which is capable of providing sub-cellular level resolution imaging *in vivo*. The simplicity, low cost, and real-time imaging performance of the HRME system have led to its use by several research groups in laboratory studies (18-31) and *in vivo* clinical investigations(32-35). However, the imaging properties of the HRME system have not been fully characterized; in particular, the axial imaging range and sensitivity to out-of-focus light have not been quantitatively studied. The purpose of this chapter is to quantitatively examine the imaging properties of the HRME system with regard to defocus in scattering media. This is important because unlike optical sectioning techniques such as confocal microscopy, the HRME system possesses no inherent ability to reject out-of-focus light. When the distal tip of the fiber bundle is placed on the tissue, fluorescence from both in-focus and out-of-focus objects will be collected by the system. Out-of-focus light could in principle reduce the signal-to-background level and result in the appearance of defocused objects in the image, which may affect the accuracy of image analysis algorithms which quantify morphological features such as nuclear size, spacing, and nuclear-to-cytoplasm ratio.

Here, the imaging performance of the HRME system was investigated both with and without the fiber bundle with regard to defocus, specifically as it relates to apparent particle size and intensity. The imaging performance of HRME was compared to a simple geometric model for a 2-D phantom, the effect of defocus (object depth) on apparent image feature size in 3-D phantoms with varying scattering coefficients was quantified, and the imaging properties of HRME were compared directly to those of confocal endomicroscopy in biological tissue *in vivo*.

2.2. Materials and methods

2.2.1 HRME system

Assembly of the HRME system has been described in detail elsewhere (18). Light from a 455 nm LED (Thorlabs M455L2), is collected by a condenser lens (Olympus Plan N 4x objective), passed through a 430-475 nm bandpass excitation filter (Semrock), reflected at a 485 nm edge dichroic beamsplitter (Chroma), to an infinity-corrected objective lens (Olympus Plan N 10x). A silica fiber-optic bundle (Sumitomo, IGN-08/30) with 720 µm imaging diameter, comprising 30,000 individual fibers each 2.1 µm in diameter with NA 0.35 is positioned with its proximal end face at the objective's working distance (Fig. 2.1 (a)).

At the distal end of the fiber, excitation light generates fluorescence from a labeled sample. With the LED at full power, the illumination intensity was measured to be 1.13 mW/mm^2 at the proximal end of the fiber and 1.03 mW/mm^2 at the distal end. Fluorescent light is collected by the fiber bundle and relayed back through the objective lens, through the dichroic mirror and 506-594 nm bandpass emission filter (Semrock), and a 150 mm focal length tube lens (Thorlabs) which images the fluorescent emission onto a CCD sensor (Point Grey Research, Grasshopper 2).

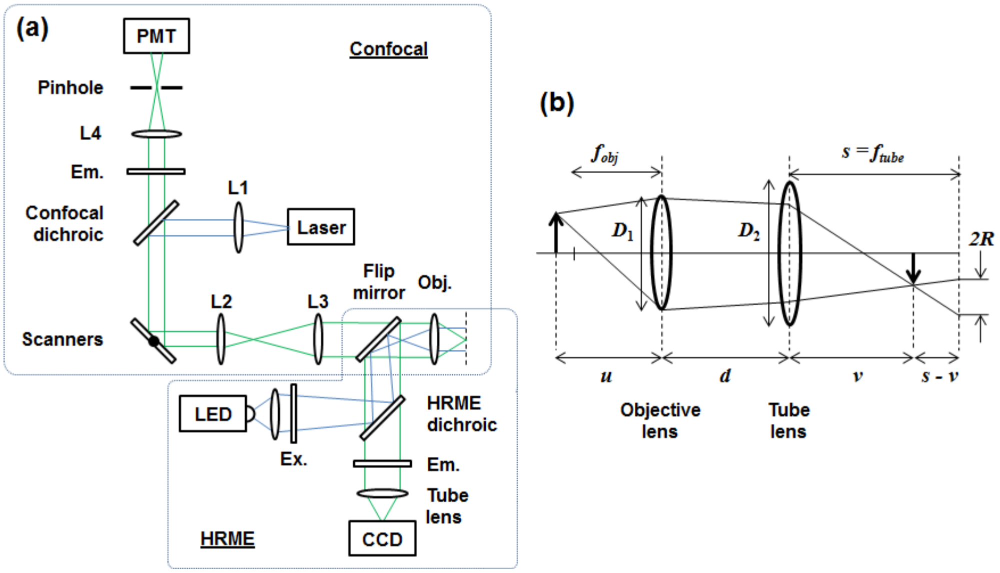
(a)
PMT
Confocal
Pinhole
L4
Em.
L1
Confocal dichroic
Laser
Flip mirror
Obj.
L2
L3
Scanners
LED
HRME dichroic
Ex.
Em.
Tube lens
HRME
CCD
(b)
f_{obj}
$s = f_{tube}$
D_1
D_2
2R
u
d
v
s - v
Objective lens
Tube lens

Fig. 2.1: Schematic diagram of the optical setup. For microendoscopy, one end of a fiber-optic bundle is placed at the working distance of the objective lens. (a) Confocal and HRME beam paths are combined with a flip mirror. L1-4: lenses, Ex: excitation filter, Em: emission filter, Obj: Objective lens. (b) Ray diagram for the geometric model used to examine HRME imaging with defocus. An object located at distance u from the objective lens (defocus of $u - f_{obj}$) will form a focused image at v, and a blurred image of radius R on the camera at $s = f_{tube}$. The objective lens and tube lens have diameters D_1 and D_2 respectively, and are separated by distance d.

2.2.2 Confocal microendoscope system

A point-scanning confocal microendoscope system was assembled (Fig. 2.1 (a)), using a 488 nm fiber-coupled laser (Blue Sky Research) for fluorescence excitation. A dichroic mirror with 488 nm edge (Semrock) and lenses L1-3 (focal lengths 35 mm, 50 mm, and 100 mm, respectively) form a collimated excitation beam, pivoting at the back aperture of the same shared 10x / 0.25 objective lens used by the HRME system. In the detection arm, fluorescent is transmitted by a separate emission filter with the same 506-594 nm bandpass range as in the HRME, focused by a 50 mm focal length lens (L4) through a 25 μm pinhole, and collected by a photomultiplier tube (Hamamatsu). The axial resolution of the confocal microendoscope was measured by removing the emission filter and recording the signal intensity as a mirror was translated away from the bundle's distal face in 1 μm increments. The distance at which the intensity dropped to half the value at contact was 6 μm. Imaging with the confocal microendoscope was performed with the fiber bundle's distal tip placed directly in contact with the sample; no additional optics were used. To enable direct comparison between images acquired with the HRME and the confocal microendoscope, the systems were coupled together with a flip mirror positioned immediately behind the objective lens to enable rapid selection of either imaging mode without repositioning the sample.

2.2.3 Geometric model

A simple geometric model was developed to predict the effect of defocus on an object's apparent size and intensity as measured by the HRME system (Fig. 2.1 (b)). The purpose of this model was to allow for comparison with experimental data, and was not an attempt to predict object depth in HRME images. This analysis was based on a model from the literature which derived an expression for the blur spot radius (R) as a function of CCD camera position (s) for a fixed object (u) (36). For the HRME system, the CCD camera is instead considered *fixed* at the focal plane of the tube lens ($s = f_{\text{tube}}$) and object position u is variable ($u - f_{obj}$ equals defocus). v is the distance from the tube lens to the image plane. Using similar triangles in Fig. 2.1 (b) and the Gaussian equation for a two lens system for *v*, we obtain:

$$R=\frac{D_1}{2}(1-dG)\left(\frac{d-G-f_{tube}}{d-G}-1\right) \quad \text{for} \quad \frac{f_{obj}D_1 d}{D_1 d+f_{obj}\left(D_1+D_2\right)}\leq u\leq\frac{f_{obj}D_1 d}{D_1 d-f_{obj}\left(D_1+D_2\right)}$$

$$R=\frac{D_2}{2}\left(\frac{d-G-f_{tube}}{d-G}-1\right) \qquad \text{otherwise, where } G=\frac{uf_{obj}}{u-f_{obj}} \tag{2.1}$$

In this model, *R* is the radius of the blurred image of a point object, formed at the camera plane. To obtain the *apparent* physical radius of the object (*AR*), we divide *R* by the system magnification, $M = f_{tube} / f_{obj}$:

$$AR=\left|\frac{R}{M}\right|=\frac{f_{obj}}{f_{tube}}|R| \tag{2.2}$$

The image formed from an extended object is the image of a point object (Eq. (2.2)) convolved with the object function, which for the experiments conducted here is a spherical fluorescent bead of 14.8 μm diameter. Due to the convolution of the blur radius with the extended object, the apparent radius of the object is equal to the sum of the object's radius and the blur radius. The apparent diameter, *AD* is twice that value, where *r* is the radius of the object:

$$AD=2\left(r+\frac{f_{obj}}{f_{tube}}|R|\right) \tag{2.3}$$

Since the total amount of light imaged onto the camera from each object is essentially constant for small amounts of defocus, we can express the light flux, *F*, from each object as:

$$F = \bar{I}_0 A_0 = \bar{I}_{blur} A_{blur} \tag{2.4}$$

where $\bar{I}_0$ is the mean intensity of the focused particle, A_0 is the area of the focused particle, $\bar{I}_{blur}$ is the mean intensity of the blurred image, A_{blur} is the area of the blurred image:

$$\overline{I}_{blur} = \overline{I}_0 \frac{r^2}{\left(r + \frac{f_{obj}}{f_{tube}} |R| \right)^2} \tag{2.5}$$

Equations 2.3 and 2.5 are used to model the apparent diameter and intensity of defocused objects in this chapter.

2.2.4 Optical phantoms

A 2-D monolayer of 14.8 µm diameter green fluorescent beads (Life Technologies, F-21010) was prepared by applying 5 µL of beads in suspension to a microscope slide and allowing the droplet to dry. The slide was mounted on a motorized translation stage (Newport MFA-CC, on-axis accuracy ± 4 µm), and images were collected with the slide located at discrete positions (*u* in Fig. 2.1 (b)) between -200 µm and +200 µm relative to the objective's focal plane (the fiber bundle was not used at this stage). Images were collected with the camera's proprietary software (FlyCap2, Point Grey Research, Firmware version 1.6.3.0); the gain was fixed at 0 dB and the exposure time was 6.59 ms. Each image was then analyzed in ImageJ (NIH version 1.46r), with each bead defined as a region-of-interest by manual segmentation using the circle tool. The diameter and mean intensity of each ROI was then calculated by analysis within ImageJ, following subtraction of the background (dark) level for each image.

Three-dimensional phantoms were made with 14.8 μm diameter green fluorescent beads dispersed within non-scattering (NS), low-scattering (LS), and high-scattering (HS) phantoms. We used an intralipid-agar phantom system which has previously been used to simulate biological tissue (37-39). 0.1 g of agar (Sigma, A9799) and 0.2 g of fluorescent beads in solution were mixed with varying amounts of DI water; 10.0 mL for the NS phantom, 9.75 mL for the LS phantom, 9.0 mL for the HS phantom. Each mixture was vortexed until the agar was dispersed, then immersed into boiling water for 10 minutes. 20% Intralipid (Sigma, I141) was then added to the fluorescent bead mixture in varying quantities; no Intralipid was added to the NS phantom, 0.25 mL was added to the LS sample, 1 mL to the HS sample (NS = 0%, LS = 0.5%, HS = 2.0% Intralipid solids). The mixture was then vortexed again, poured into a 60 mm diameter petri dish and allowed to cool to room temperature overnight. A spatial frequency domain imaging system (40) was used to measure the reduced scattering coefficients of the phantoms containing Intralipid, obtaining values of 1.08 mm^{-1} and 2.54 mm^{-1} for the low and high scattering phantoms, respectively, at a wavelength of 520 nm.

2.2.5 Three-dimensional imaging

The agar phantoms were mounted on the same motorized stage as used for the 2-D phantoms and translated such that a focused image of the phantom surface was seen on the HRME camera. This location was then considered to be depth $z = 0$ for the phantom under study. Images were then collected as the phantom was moved toward the objective lens in 10 μm steps, with fluorescent beads at different depths moving through the focal plane. Several axial scans at different lateral regions were collected, allowing us to obtain image data from beads located at a range of depths within each phantom. Images were collected at 0 dB gain and exposure times of 5.00 ms, 6.00 ms, and 3.00 ms, respectively, for the NS, LS, and HS samples.

2.2.6 Fiber-optic imaging

For imaging with the complete HRME system, the fiber bundle was placed in the system with its proximal end at the working distance of the objective lens. The distal end of the bundle was brought into gentle contact with the surface of the agar phantoms and images were acquired at several different lateral regions on the phantom surface. Each of these regions was then imaged *without* the fiber bundle, with images taken over an axial scan range as described in section 2.2.5. The same field-of-view in the sample was located by placing an ink mark on the sample surface adjacent to the fiber bundle tip, for guidance to the same region when the fiber bundle was removed. The exact same region was then identified by carefully searching visually for the same distribution of fluorescent beads. This process allowed the depth of each fluorescent bead in the fiber-optic bundle images to be determined without physically advancing the bundle into the phantom. Fiber-optic HRME images were taken with 0 dB camera gain and 15.00 ms exposure. The non-fiber-optic images were taken at the same exposure settings as described in section 2.2.5; 5.00 ms, 6.00 ms, and 3.00 ms, respectively, for the NS, LS, and HS samples.

2.2.7 In-vivo imaging

Images of normal human oral mucosa were acquired with the HRME and confocal microendoscope, following topical application of proflavine solution (0.01% w/v in sterile

PBS). Images with each system were recorded in quick succession by use of the flip mirror (Fig. 2.1 (a)). Human subject imaging was performed under a protocol approved by the Rutgers University IRB.

2.3. Results

2.3.1 Epi-fluorescence imaging of phantoms

Figure 2.2 shows images of a 2-D monolayer of fluorescent beads imaged with the HRME (panels a-d) and the confocal microendoscope (panels e-h), as a function of defocus. It can be seen that with HRME, the apparent diameter of the beads increases, and mean intensity rapidly decreases with defocus, leading to nearly uniform background intensity for defocus greater than approximately 250 μm. With confocal microendoscopy, as expected, the intensity of out-of-focus beads is rapidly attenuated, preventing significant elevation of background arising from defocused objects.

Figures 2.2 (i) and 2.2 (j) quantify the apparent diameter and mean intensity, respectively, of 14.8 μm fluorescent beads as a function of defocus when imaged with HRME, alongside the theoretical predictions from the geometric model described in section 2.2.3. Good agreement between the measured bead diameters and predicted values supports our use of manual delineation of beads.

Figure 2.3 shows the apparent diameter and mean intensity of fluorescent beads as a function of bead depth within thick 3-D phantoms. These images were acquired without the fiber bundle, with the surface of the phantom positioned at the working distance of the HRME objective lens; “bead depth” is thus equivalent to defocus. These results maintain good agreement with predictions from the geometric model under all three levels of scattering tested, even though the model neglects the effects of scattering. Here, the reduced scattering coefficients are on the order of cm^{-1}, whereas defocus reduces the imaged mean object intensity significantly over distances on the order of tens of micrometers. A 50% reduction in mean intensity occurs with defocus of approximately 5 µm and a 90% reduction in mean intensity after approximately 25 µm (Fig. 2.3 (d-f)). While it appears that higher levels of scattering reduce the maximum achievable imaging depth (NS ~ 500 µm, LS ~ 300 µm, HS ~ 250 µm), the effect of scattering at levels simulating biological tissue appears small compared to the effect of defocus; the predicted mean intensity of a bead located at a depth (defocus) of 240 µm is only ~1% of that of a bead located at the surface (in focus).

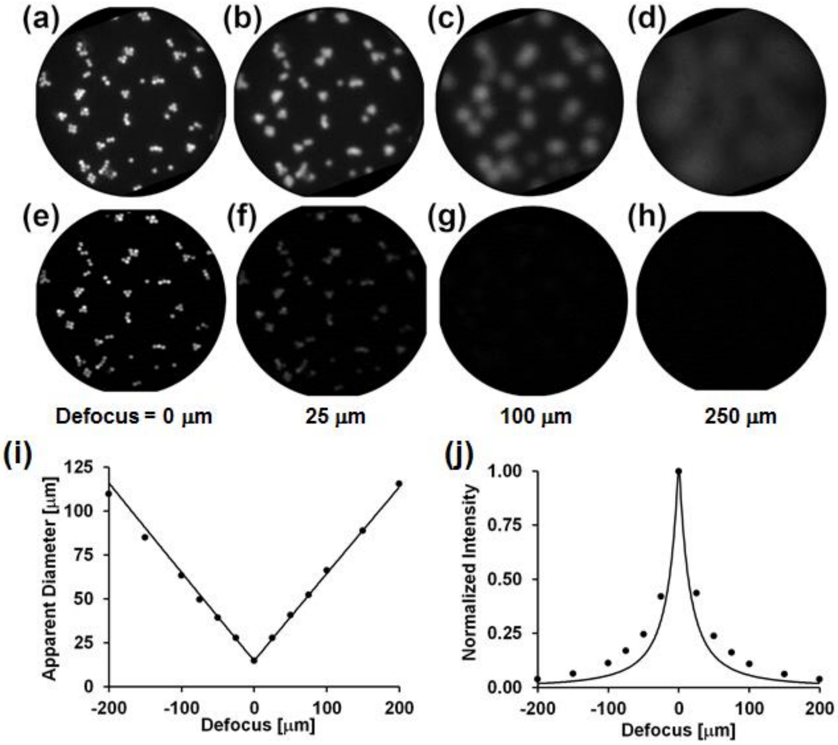

Fig. 2.2: HRME (a-d) and confocal microendoscopy (e-h) imaging of a monolayer of 14.8 μm diameter beads as a function of defocus (distance from the monolayer to the fiber bundle's distal tip). All images are 720 μm in diameter. (i) Measured (dots) and theoretical prediction (line) for bead diameter as a function of defocus. (j) Measured (dots) and theoretical prediction (line) for the mean bead intensity as a function of defocus.

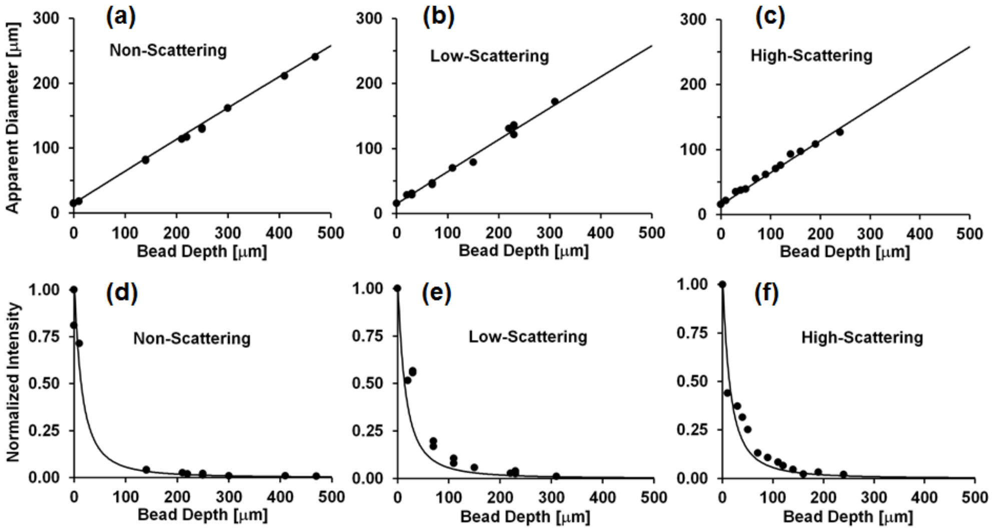

Fig. 2.3: (a,b,c) Apparent diameter of 14.8 μm fluorescent beads in NS, LS, and HS phantoms as a function of bead depth beneath the phantom surface. (d,e,f) Normalized mean intensity of imaged fluorescent beads as a function of depth beneath the phantom surface in NS, LS, and HS samples. Circles: experimental data, line: predicted values from model.

2.3.2 Fiber-optic HRME imaging of 3-D phantoms

Figure 2.4 presents a side-by-side comparison of 3-D phantom imaging with the HRME, both without (Fig. 2.4 (a-c)) and with the fiber-optic bundle (Fig. 2.4 (d-f)). All images have been brightened by the same amount in order to make the dimmer beads more apparent. Figure 2.4 (g-i) shows the apparent diameter of the beads in the HRME images as a function of bead depth within the 3-D phantom. Fig 2.4 (j-l) shows the normalized mean intensity of the beads in the HRME images as a function of bead depth. These data suggest that the HRME fiber-bundle based system displays similar imaging performance with respect to the effect of defocus, to the epi-fluorescence microscope; the fiber bundle confers no sectioning ability.

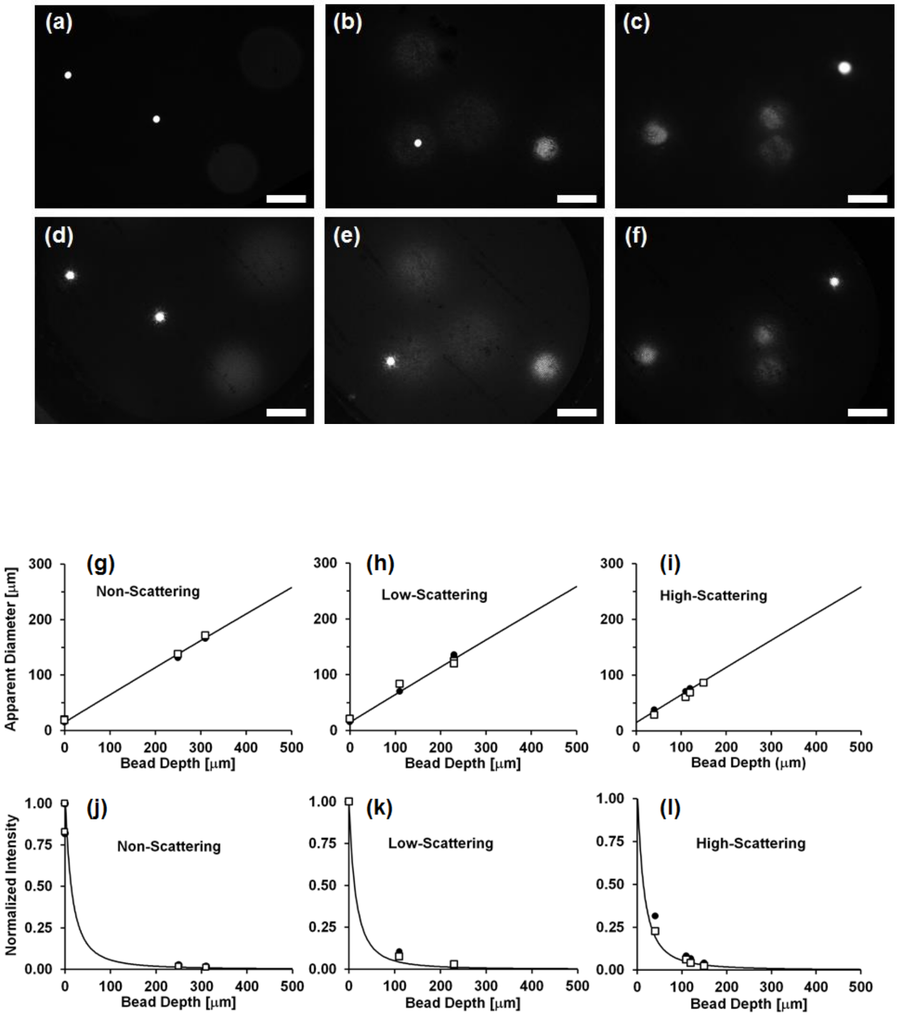

Fig. 2.4: (a-f) Comparison between images of 3-D phantoms taken without (a-c) and with the fiber bundle (d-f) in NS (a,d), LS (b,e), and HS (c,f) samples. Scale bar = 100 µm. (g-i) Apparent diameter at surface of 14.8 µm fluorescent beads in NS, LS, and HS phantoms. (j-l) Normalized intensity at phantom surface in NS, LS, and HS samples.

(Squares: data from fiber optic images, circles: data from non-fiber-optic images, solid line: expected values from model).

2.3.3 Comparison of HRME and confocal microendoscopy

Figure 2.5 shows images of *in vivo* human oral mucosa taken using the HRME system (Fig. 2.5 (a)) and confocal microendoscopy (Fig. 2.5 (b)). These images were acquired nearly simultaneously, with the only delay arising from activating the flip mirror which allowed the system to be switched between (Fig. 2.1 (a)). Following staining with topical proflavine (0.01% w/v), cell nuclei appear as discrete bright dots within each image. The confocal image (Fig. 2.5 (b)) appears to exhibit lower background and higher contrast which allows nuclei to be identified more easily in regions which have more crowded or overlying cells. However, the HRME still retains the ability to resolve nuclear detail in most parts of the image, without being adversely affected by defocused objects.

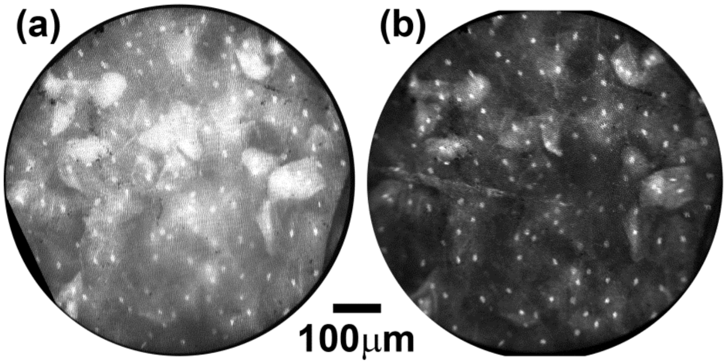

Fig. 2.5: *In vivo* imaging of human oral mucosa following topical application of proflavine, using HRME (a) and confocal microendoscope systems (b).

2.4. Discussion & Conclusions

The axial response of a recently developed high-resolution microendoscope (HRME) system was quantified for the first time, using a series of optical phantoms. These phantoms were designed to simulate fluorescently labeled nuclei distributed at varying depths within scattering tissue, mimicking the proflavine-stained epithelium imaged in earlier HRME studies. The HRME has no optical sectioning ability with which to eliminate out-of-focus light when imaging thick tissue, but nevertheless can clearly delineate epithelial nuclei in normal and neoplastic tissues (33-35). This study showed that the HRME system produces images of deep lying (defocused) objects with apparent diameters as predicted by a simple geometric model. This could in principle lead to the apparent size of deep nuclei being mistakenly overestimated by morphologic analysis algorithms. However, the average intensity of defocused objects was also shown to rapidly decrease with defocus within a few 100 μm. In a scattering matrix, the intensity of defocused objects attenuated even more rapidly, resulting in a non-zero background level contributing to HRME images, but not sufficient to reduce contrast of the most superficial nuclei.

Confocal endomicroscopy appears to provide higher contrast than HRME when nuclei are particularly crowded, and can offer the ability to examine tissue across the full thickness of the epithelium. Use of fluorescent contrast agents such as fluorescein and indocyanine green which distribute non-specifically throughout tissue would also benefit from the ability of confocal methods to prevent out-of-focus light from reaching the detector and lowering contrast. Interestingly, the findings reported in this chapter appear complementary to those of El Hallani *et al.*, who recently demonstrated that independent of imaging system, limited diffusion of the proflavine contrast agent restricts imaging to depths of only 50-100 μm in epithelial tissues (41). Thus it would appear that the effects of defocus shown here, in addition to the biodistribution of contrast agent, both enable HRME to effectively resolve cell nuclei within only the most superficial layers of the epithelium with minimal effect from out of focus light. Previous and future studies which quantify nuclear morphology for tissue classification (22, 32-34), should not be adversely affected by fluorescence from nuclei located deeper within the epithelium.

Chapter 3: Integration of Structured Illumination With HRME for Optical Sectioning

3.1. Introduction

As mentioned previously, HRME cannot effectively image tissues stained with highly penetrating or systemically delivered non-specific fluorescent dyes because it has no method of removing the resulting OOF light. Structured illumination microscopy (SIM) is a technique which has been shown to exhibit optical sectioning (42, 43). As mentioned previously, optical sectioning is the property of rejecting OOF light and is usually associated with confocal and multiphoton microscopy. Unlike these techniques however, SIM does not require laser excitation, raster scanning, or the use of a pinhole to reject the OOF light. Instead SIM achieves optical sectioning by introducing a high spatial frequency pattern into the illumination path (hence the name "Structured Illumination") and computationally processing a sequence of images captured under different pattern conditions. Within this chapter, the structured illumination principle was combined with the high-resolution microendoscope platform (25) to provide HRME with optical sectioning ability.

SIM was introduced in 1997 by Neil, Juškaitis, and Wilson (42). The theoretical explanation given here is largely based on the framework described in that paper and from a 2007 paper from Chasles, Dubertret, and Boccara (43). The SI concept has subsequently been used by several labs both for optical (axial) sectioning (44, 45) and for (lateral) super-resolution imaging (46-52). SI microscopy is achieved by interposing a one dimensional grid (stripe pattern) into the illumination path with some means of laterally shifting the pattern by a fraction of the grid period. This may be achieved by mounting a chrome-on-glass grid onto a precision translation stage, or alternatively by creating the grid pattern with a spatial light modulator. Fig. 3.1 is a schematic of the SI microscope system.

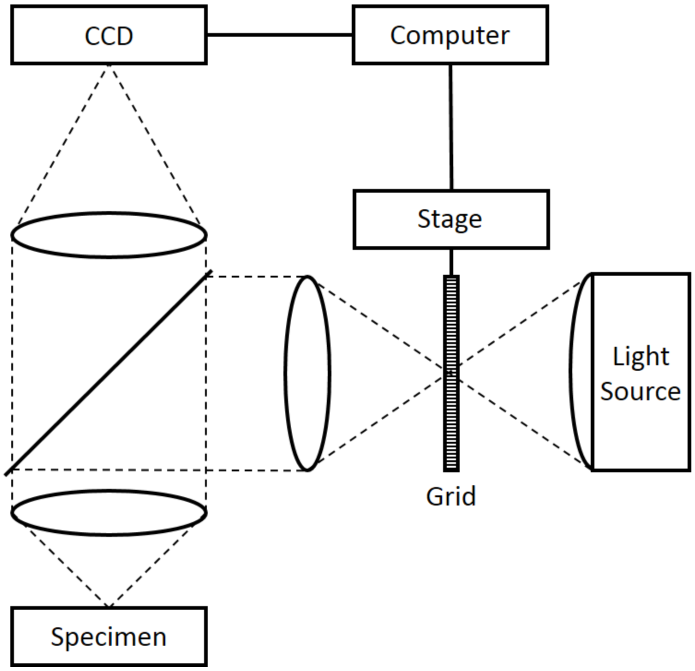

Fig. 3.1: An example schematic of a SIM system

3.2 Theoretical Basis of Structured Illumination Microscopy

SIM achieves optical sectioning because high spatial frequencies are more strongly attenuated with defocus (small features disappear more quickly than large features as an object moves out of focus). Therefore, when properly focused (i.e. when the grid is imaged precisely at the focal plane of the microscope), the grid pattern will only appear sharp near the focal plane and will be rapidly attenuated at locations above or below this plane (the rate of attenuation will depend on the spatial frequency of the grid). The transmission of the grid can be written:

$$S(t_0, w_0) = \frac{1}{2}\left(1 + m\cos\left(\tilde{v}t_0 + \phi\right)\right) \tag{3.1}$$

where m is the modulation depth (contrast of the sinusoid), t_0 and w_0 are the optical coordinates, related to the real coordinates by $(t, w) = \mathrm{NA}(2\pi/\lambda)(x, y)$, and φ is an arbitrary spatial phase. $\tilde{v}$ is the normalized spatial frequency, which is related to the actual spatial frequency by $\tilde{v} = \beta\lambda v/\mathrm{NA}$, where β is the magnification between the grid plane and the image plane. λ is the wavelength of the light, v is the actual spatial frequency, and NA is the numerical aperture of the objective lens. If the grid S given in Eq. (3.1) is imaged onto an object with reflectance (or fluorescence or transmittance) $\tau(t_1,w_1)$, the image collected by the camera is given by:

$$\begin{aligned} I\left(t, w\right) = \iint S\left(t_0, w_0\right)\Big|\iint h_1\left(t_0 + t_1, w_0 + w_1\right) \\ \times \tau(t_1, w_1)\,\mathrm{h}_2\left(t_1 + t, w_1 + w\right) dt_1 dw_1\Big|^2 dt_0 dw_0 \end{aligned} \tag{3.2}$$

By collecting three images, I_1, I_2, and I_3, with lateral phase shifts $\varphi_0 = 0$, $2\pi/3$, and $4\pi/3$, respectively and combining the images according to:

$$I_p = k\sqrt{(I_1 - I_2)^2 + (\mathrm{I}_1 - \mathrm{I}_3)^2 + (\mathrm{I}_2 - \mathrm{I}_3)^2} \tag{3.3}$$

we obtain an optically sectioned image (I_p), where k is an arbitrary constant. To illustrate this result, Fig. 3.2 (a) shows three sinusoidal patterns with $\tilde{v}$ equal to one and $\varphi = 0$, $2\pi/3$, $4\pi/3$. These can be interpreted as the illumination intensity at the sample when a grid with sinusoidal transmission is used. Fig. 3.2 (b) demonstrates that by using Eq. 3.3 with three images acquired using the above phase shifts, the grid pattern can be removed from the final reconstructed image.

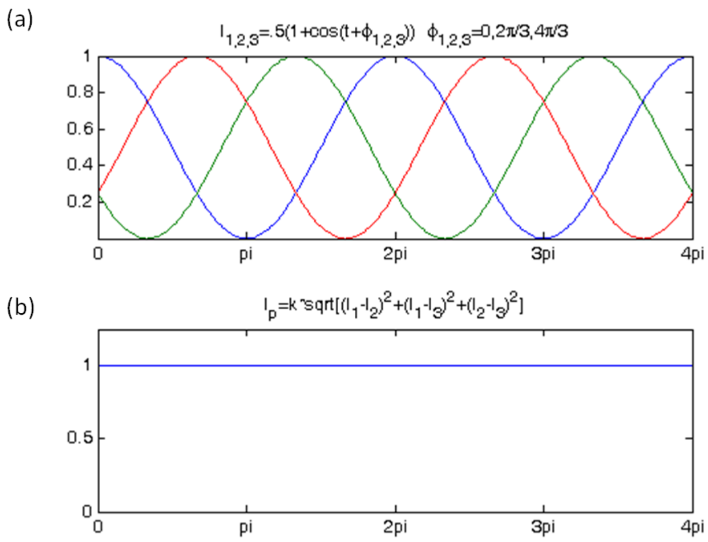

Fig. 3.2: (a) Three sinusoids in form of Eq. 3.1. (b) The same three sinusoids recombined according to Eq. 3.3.

The efficiency with which the grid pattern is imaged onto the object plane is given by the weak object transfer function (WOTF) $g(u,\tilde{v})$, which is commonly approximated using the Stokseth approximation (53), given in Neil, Juškaitis, and Wilson (42) as:

$$g(u,\tilde{v}) = f(\tilde{v})\left\{2\frac{J_1\left[u\tilde{v}(1-\tilde{v}/2)\right]}{\left[u\tilde{v}\left(1-\tilde{v}/2\right)\right]}\right\} \tag{3.4}$$

where J_1 is a Bessel function of the first kind, u is the normalized defocus, related to the actual defocus z by $u = 8(\pi/\lambda)z\sin^2(\alpha/2)$, and:

$$f(\tilde{v}) = 1 - 0.69\tilde{v} + 0.0076\tilde{v}^2 + 0.043\tilde{v}^3 \tag{3.5}$$

The quantity $g(u,\tilde{v})$ is directly proportional to the image intensity for any given location within the image and this is what generates the optical sectioning effect in SIM. We can therefore predict the thickness of the optical section from Eq. 3.4. Fig. 3.3 (a) shows the intensity predicted by the WOTF (Eq. 3.4) for a uniform plane object, as a function of object defocus when a 10 lp/mm grid ($\tilde{v}$ = 0.0455) is used. The object defocus distance required to reduce the detected intensity by one half is a commonly used measure of sectioning strength known as the full-width, half-maximum (FWHM). Fig. 3.3 (b) shows the predicted FWHM for different values of normalized grid frequency, $\tilde{v}$. The predicted value goes to infinity as the $\tilde{v}$ approaches 0 and 2 with a minimum at $\tilde{v}$ = 1 and a broad flat region from approximately $\tilde{v}$ = 0.5 to $\tilde{v}$ = 1.5.

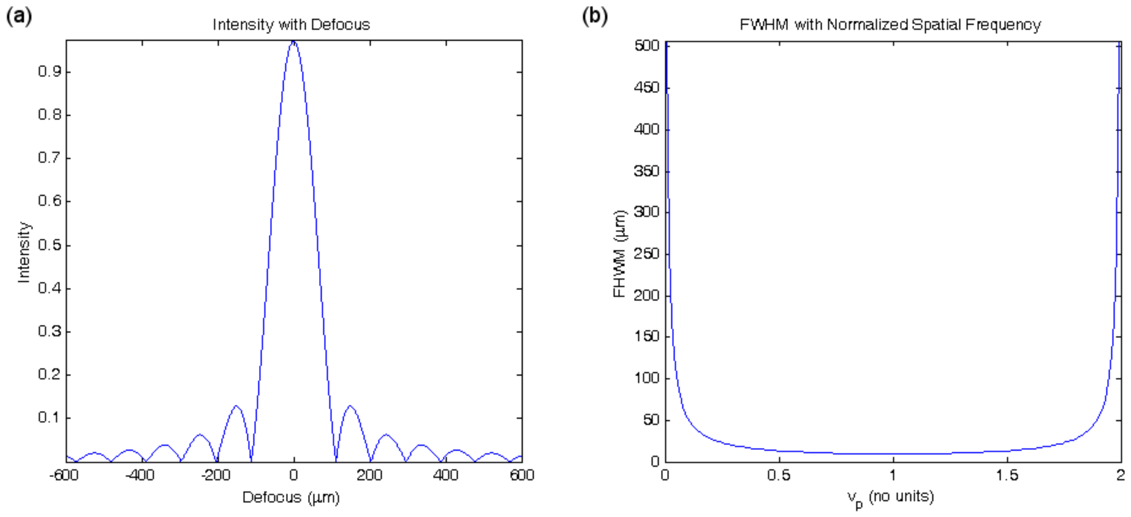

Fig. 3.3: (a) Theoretical curve demonstrating image attenuation with axial defocus using SIM. (b) Theoretical FWHM of the curve shown in (a) as a function of normalized grid spatial frequency.

Additionally, we can also achieve SIM using square wave illumination intensity, instead of a sinusoid as shown in Fig. 3.4. The experimental section of this chapter will use chrome-on-glass Ronchi rulings with a square wave transmission profile to generate periodic illumination at the sample.

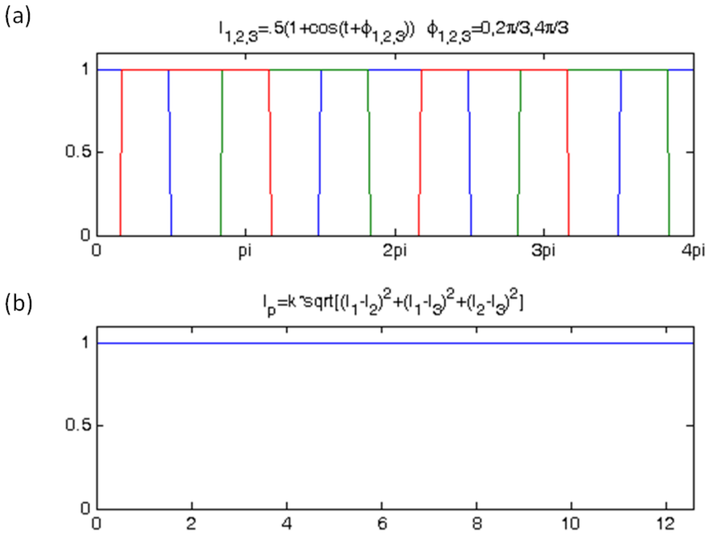

Fig. 3.4: (a) 3 square waves with relative phase shifts of $\phi = 0$, $2\pi/3$, and $4\pi/3$. (b) Square waves combined according to Eq. 3.3

3.3 SIM System

The assembly of the SIM system is very similar to the assembly of the HRME system which has been previously described in Chapter 2 of this thesis and reference (25). A schematic of the SIM system is shown in Fig. 3.5. The difference between HRME and SI-HRME is that a Ronchi ruling with 10 or 40 line pairs per mm (lp/mm) is placed at the focal plane of the condenser (or "grid") lens (Olympus objective RMS4X). (A 10x/0.25 objective is still used for imaging the specimen). The Ronchi ruling slide was mounted on a precision motorized translation stage (Zaber) which controls the lateral translation (and spatial phase, ϕ) of the grid pattern. For the 10 lp/mm ruling (period 0.1 mm, normalized frequency ($\tilde{\nu}$) = 0.06), phase shifts of $\phi = 2/3\pi$ and $4/3\pi$ corresponded to actual lateral shifts of 33.3 μm and 66.6 μm, respectively. For the 40 lp/mm ruling (period 0.025 mm, normalized frequency ($\tilde{\nu}$) = 0.22), phase shifts of $\phi = 2/3\pi$ and $4/3\pi$ corresponded to actual lateral shifts of 8.3 μm and 16.3 μm, respectively.

Because the camera acquisition and grid stage phase shifting must be tightly synchronized, custom LabVIEW code was written to control the camera and grid stage; this code also implements the SIM reconstruction algorithm (Eq. 3.3) and saves the images.

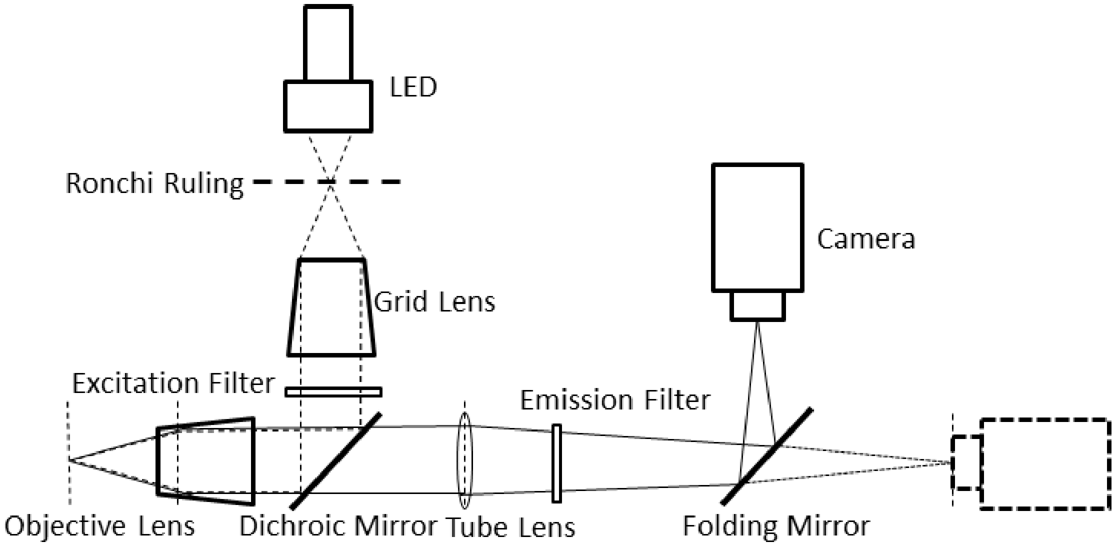
LED
Ronchi Ruling
Camera
Grid Lens
Excitation Filter
Emission Filter
Objective Lens
Dichroic Mirror
Tube Lens
Folding Mirror

Fig. 3.5: Schematic of the SI-HRME microscope assembled here. For microendoscopic imaging, the fiber-optic bundle is placed at the working distance of the objective lens.

3.4 Programming

In order to generate SI images there are four vital functions which must be performed. Images must be collected, the grid pattern must be translated, the three phase-shifted images must be recombined on a pixel-by-pixel basis, and the resulting image must be displayed or saved. Perhaps the most obvious way to accomplish this is to collect the three phase-shifted images in sequence as shown in Fig. 3.6 (a). In this algorithm, the three images are collected ($\phi = 0, 2/3\pi, 4/3\pi$) then the translation stage returns to the initial position ($\phi = 0$). When not collecting SI images the camera will collect in continuous video mode. By looping the SI image collection (i.e. collecting the three images and returning the stage to the initial position), SI images can be continuously displayed as they become available. This is shown in Fig. 3.6 (b). As an improvement to this program, upon collection of the third image ($\phi = 4/3\pi$), the direction of the shift can be reversed and the $\phi = 2/3\pi$ image can be collected on the reverse trip rather than cycling back to $\phi = 0$, thus reducing the number of grid translations per SI image. A schematic of this algorithm is shown in Fig. 3.6 (c). When looped, the program in Fig 3.6 (b) requires 4 shifts to create 1 image, in contrast the program in Fig. 3.6 (c) creates 2 SI images for every 4 shifts. A final program continuously shifts in the same direction through the entire range of motion of the translation stage, creating an image at each position by using the last 3 images (i.e. images are output at $\phi = 4/3\pi, 2\pi, 8\pi/3$, etc.) , shown in Fig. 3.6 (d). The speed of these algorithms was tested by looping the collection of 10 images and measuring the time required to collect the images. The first continuous program (Fig. 3.6 (b)) took 9.335 s to collect the 10 images, the second 6.725 s, the third 3.191 s. The optically sectioned imaging rate for these three programs are 1.07, 1.49, and 3.13 frames per second, respectively.

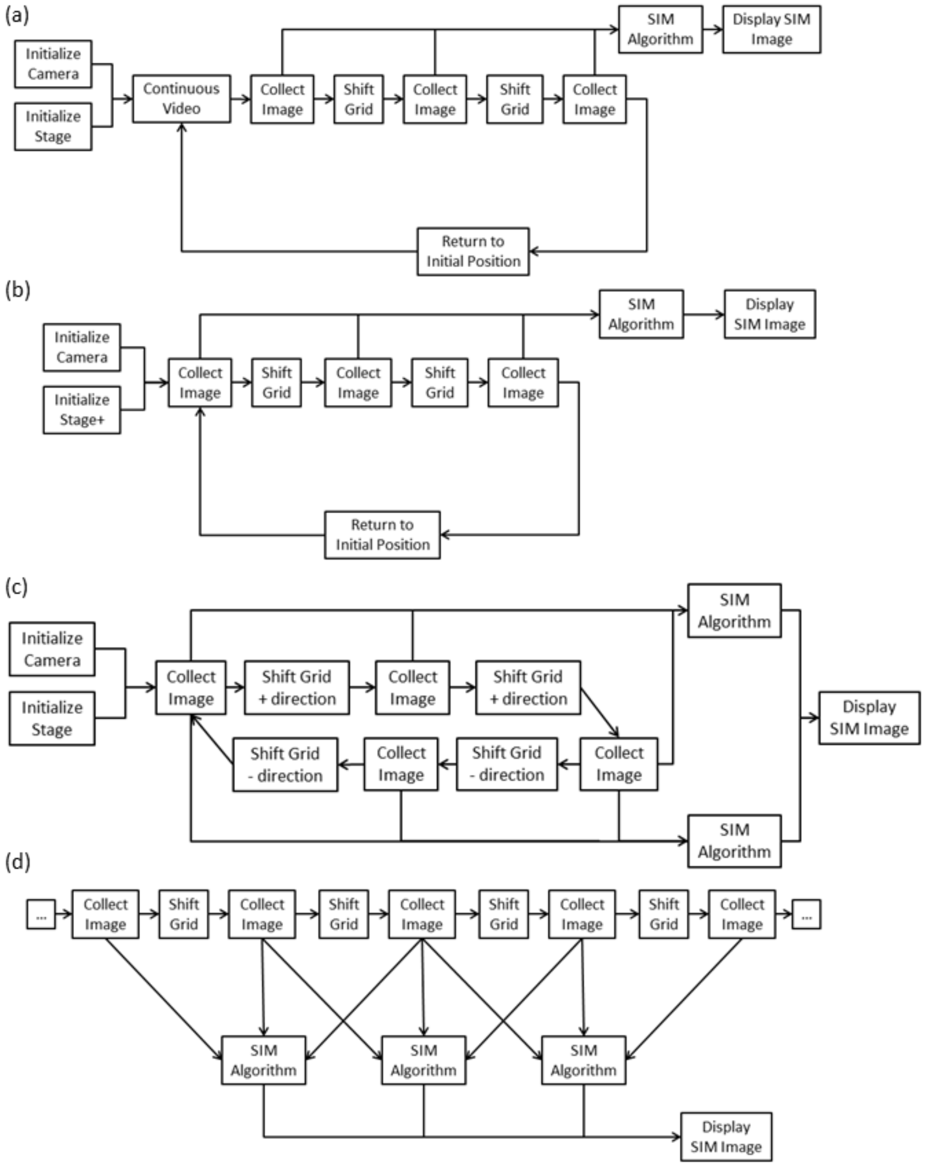
(a)
Initialize Camera
Initialize Stage
Continuous Video
Collect Image
Shift Grid
Collect Image
Shift Grid
Collect Image
SIM Algorithm
Display SIM Image
Return to Initial Position
(b)
Initialize Camera
Initialize Stage+
Collect Image
Shift Grid
Collect Image
Shift Grid
Collect Image
SIM Algorithm
Display SIM Image
Return to Initial Position
(c)
Initialize Camera
Initialize Stage
Collect Image
Shift Grid + direction
Collect Image
Shift Grid + direction
Collect Image
Shift Grid - direction
Collect Image
Shift Grid - direction
SIM Algorithm
SIM Algorithm
Display SIM Image
(d)
...
Collect Image
Shift Grid
Collect Image
Shift Grid
Collect Image
Shift Grid
Collect Image
Shift Grid
Collect Image
...
SIM Algorithm
SIM Algorithm
SIM Algorithm
Display SIM Image

Fig. 3.6: Flow diagrams demonstrating various algorithms for SI programming. (a) Single SI image collection. (b) Step-step-return image collection. (c) Back and forth image collection. (d) Continuous image collection.

3.5 System Validation

In order to measure the optical sectioning power of the SI microscope, a thin fluorescent plane object was axially translated through the focal plane of the microscope system. A thin fluorescent sample was created by placing a 10 µL drop of fluorescein solution (Fluorescein sodium salt, Sigma-Aldrich, F6377, 5 mg/mL in deionized water) on a microscope slide (VWR VistaVision 75x25x1 mm) which was then covered with a cover slip (VWR micro cover glass, 22x30 mm, No.2). This would be expected to create a 15 µm thick layer of the fluorescein solution (volume = 10 µL = 10 mm^3, area of slide = 660 mm^2, 10 mm^3/660 mm^2 = 0.015 mm = 15 µm). This slide was mounted on a precision translation stage (Newport MCA-CC) controlled by a motion controller (Newport ESP301 Motion Controller). The fluorescent plane was brought into focus by imaging the grid onto the fluorescent plane (i.e. the grid was projected onto the object plane of the camera, so when the grid is in focus, the sample is in focus). The z-position was zeroed, then the stage was moved far from the focal plane (500 µm for the 10 lp/mm grid in 5 µm steps, 200 µm for the 40 lp/mm grid in 1 µm steps). The results of these experiments are shown in Fig. 3.7. Fig. 3.7 (a) shows a 15 µm thick plane modeled as a step function, Fig 3.7 (b) shows the WOTF predicted from Eq. 3.4 for grid frequencies of 10 lp/mm (blue) and 40 lp/mm (green). The expected FWHM while imaging this object is given by convolving the WOTF with the object (step function). Actual data compared with predicted behavior is shown in Fig. 3.7 (c) and Fig. 3.7 (d) for 10 lp/mm and 40 lp/mm respectively. The measured FWHM for 10 lp/mm and 40 lp/mm grids are less than the theoretical prediction by 10.9% and 10.7%, respectively. The decreased FWHM section thickness may be due to the decreased modulation depth of the system (i.e. m < 1 in Eq. 3.1) or there may be a small difference between the focal plane of the camera and the plane where the grid is brought into focus.

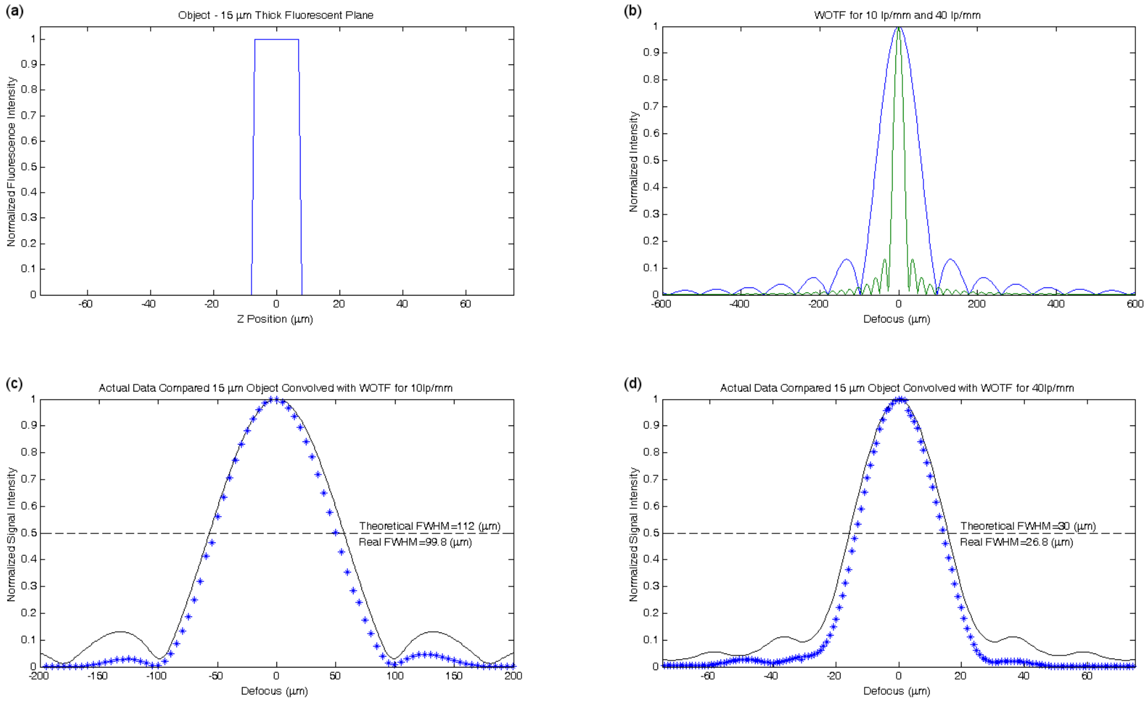

Fig. 3.7: (a) Intensity profile of a 15 μm thick object plane. (b) Expected response of the SI system to an infinitely thin plane object at varying defocus, for 10 lp/mm (blue) and 40 lp/mm (green) grids. (c) Experimental data (points) from the 10 lp/mm SIM compared to theory (solid line). (d) Experimental data (points) from the 40 lp/mm SIM compared to theory (solid line).

Example SI images are shown in Fig. 3.8. Each image shows approximately the same field of view on a sample of lens paper labeled with a fluorescent highlighter. In Fig. 3.8 (a), a standard wide-field epi-fluorescence image is shown and as can be seen, there are in-focus and out-of-focus paper fibers and there are regions of the image (indicated by white arrows) where there are no resolvable fibers, these regions contribute a measureable signal which results in a loss of contrast in the image (i.e. a “graying” of the background). By comparison, Fig. 3.8 (b) and Fig. 3.8 (c) show optically sectioned SI images with 10 lp/mm and 40 lp/mm grids, respectively. As can be seen, in the 10 lp/mm image (Fig. 3.8 (b)) the farthest out-of-focus fibers have been attenuated or removed altogether, and in the 40 lp/mm image (Fig. 3.8 (c)), the signal from an even greater number of out-of-focus fibers has been partially or completely attenuated. Furthermore, background fluorescence is completely removed in Fig. 3.8 (b) and Fig. 3.8 (c) (compare the area indicated by the white arrow in Fig. 3.8 (a-c)). Since the grid pattern cannot be imaged onto this region (there is no sample structure on which to image it), this region of the image is not modulated when the grid pattern is shifted; therefore, when the difference between the images is taken (Eq. 3.3), nothing remains. Fig. 3.8 (d-f) show images of 15 µm fluorescent particles in a monolayer on a microscope slide taken under conventional epi-fluorescence, SIM with the 10 lp/mm grid, and SIM with the 40 lp/mm grid, respectively. Because the 10 lp/mm SIM image optical section thickness is much larger than the thickness of the particle monolayer, we can see that there is no difference between the Non-SIM and 10 lp/mm SIM images other than the brightness. In contrast, the upper right corner of Fig. 3.8 (f) (40 lp/mm SIM) is obviously darker than the rest of the image. This indicates that the 40 lp/mm grid was not efficiently imaged onto this portion of the sample. This is most likely due to a small misalignment in either the Ronchi ruling, the sample, or both.

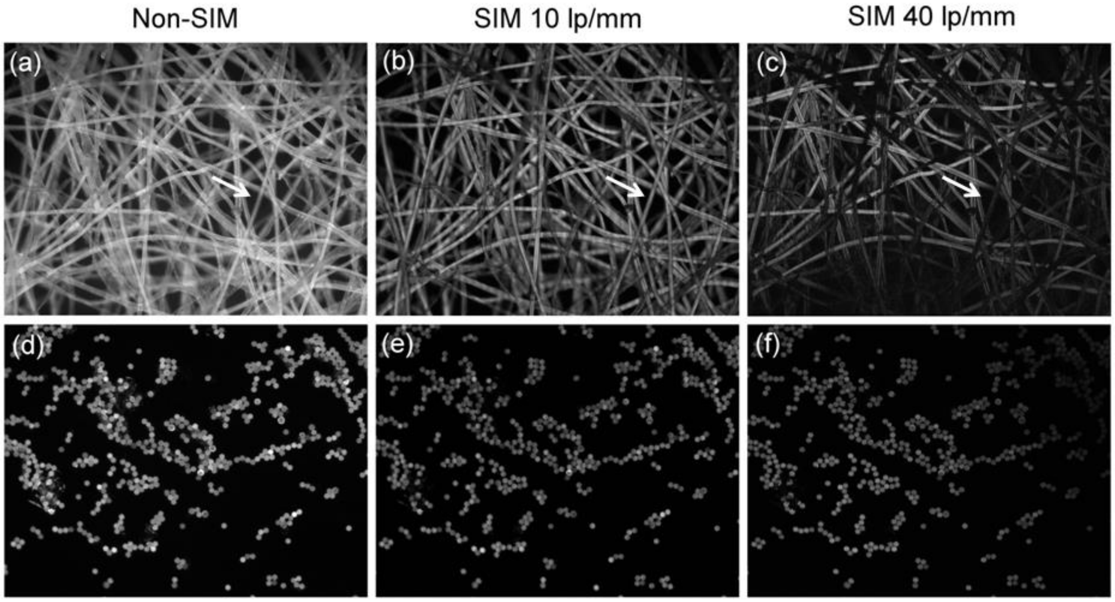

Fig. 3.8: Example SI images, compared with standard fluorescence imaging. (a-c) Lens paper labeled with fluorescent pen, non-SIM, SIM 10 lp/mm, and SIM 40 lp/mm, respectively. (d-f) 15 µm fluorescent beads in a monolayer; non-SIM, SIM 10 lp/mm, SIM 40 lp/mm, respectively.

Fig. 3.9 (a-c) shows images of standard epi-fluorescence HRME, 10 lp/mm SIM microendoscopy, and 40 lp/mm SIM microendoscopy images, respectively. The white box indicates the same feature in each image. It is clear from these images that SI continues to provide optical sectioning when imaging through a fiber bundle, even though the periodic illumination pattern created by the Ronchi grid is delivered to the sample with reduced resolution, due to the discrete individual fibers of the bundle.

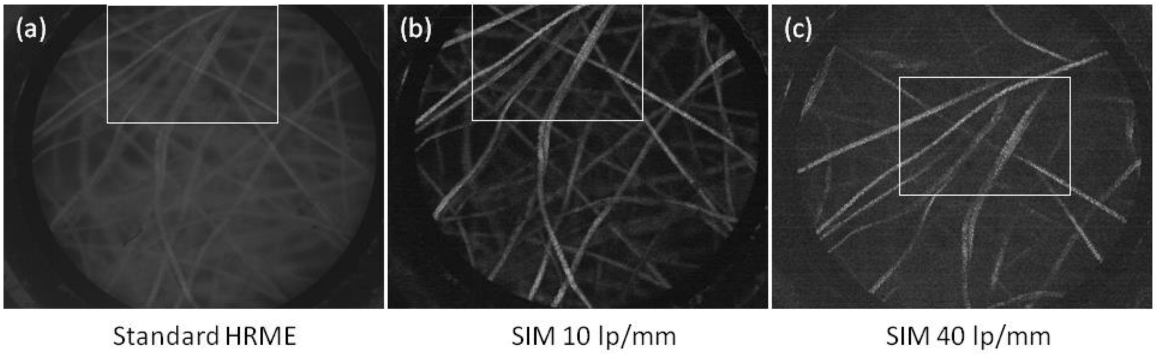

Fig. 3.9: (a) Standard HRME image of fluorescently labeled lens paper (b) SI-HRME imaging with a 10 lp/mm grid, and (c) with a 40 lp/mm grid. The regions indicated by the white boxes correspond to the same field on the sample.

3.6 Image Artifacts

The primary drawback of SI imaging is that even a small inaccuracy in the lateral phase shifting of the grid pattern results in a residual grid pattern appearing in the image. Fig. 3.10 shows mathematically generated sinusoids with zero phase error (Fig. 3.10 (a)) and 5% phase error in one of the two shifts (zero to $2/3\pi$ *or* $2/3\pi$ to $4/3\pi$), (Fig. 3.10 (b)). Fig. 3.10 (c) and Fig. 3.10 (d) show the resulting profiles when the SIM algorithm is applied to the sinusoids with zero phase error (Fig. 3.10 (c)) and with phase error (Fig. 3.10 (d)). It is apparent from this simple simulation that a relatively small lateral error in the placement of the grid will result in a noticeable artifact in the reconstructed image.

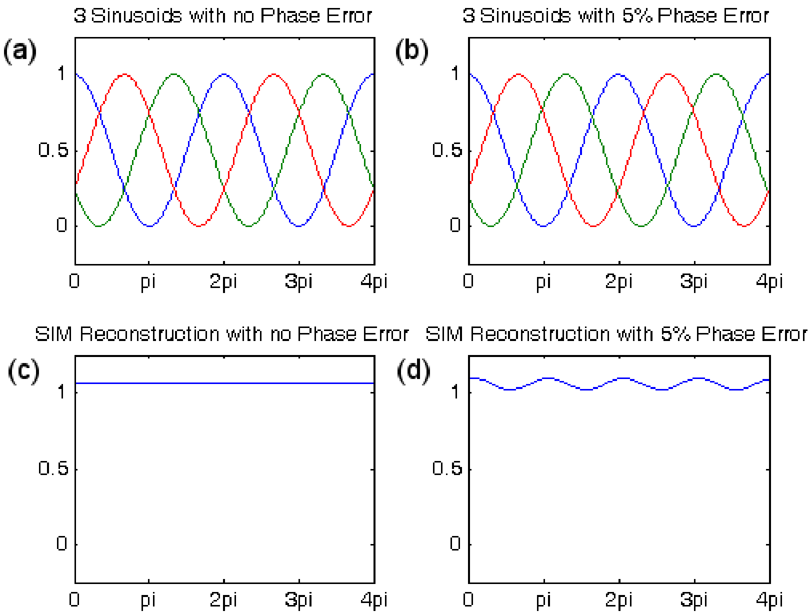

Fig. 3.10: (a) Three sinusoids with no phase shift error. (b) Three sinusoids with 5% phase shift error. (c) Three sinusoids recontructed using the SIM algorithm with zero phase error. (d) Three sinusoids recontructed using SIM algorithm with 5% error in one of the two shifts.

Fig. 3.11 (a) and Fig. 3.11 (b) show SI images collected in reflectance on a plane mirror surface using 10 lp/mm and 40 lp/mm grids, respectively. The residual grid pattern is apparent in both images. In order to minimize this artifact, it is necessary to ensure that the placement of the grid is as accurate as possible. Additionally, it must be mentioned that the sample must remain motionless during the collection of the three images for reconstruction, otherwise the field of view will not be consistent through the three images and will therefore not be comparable.

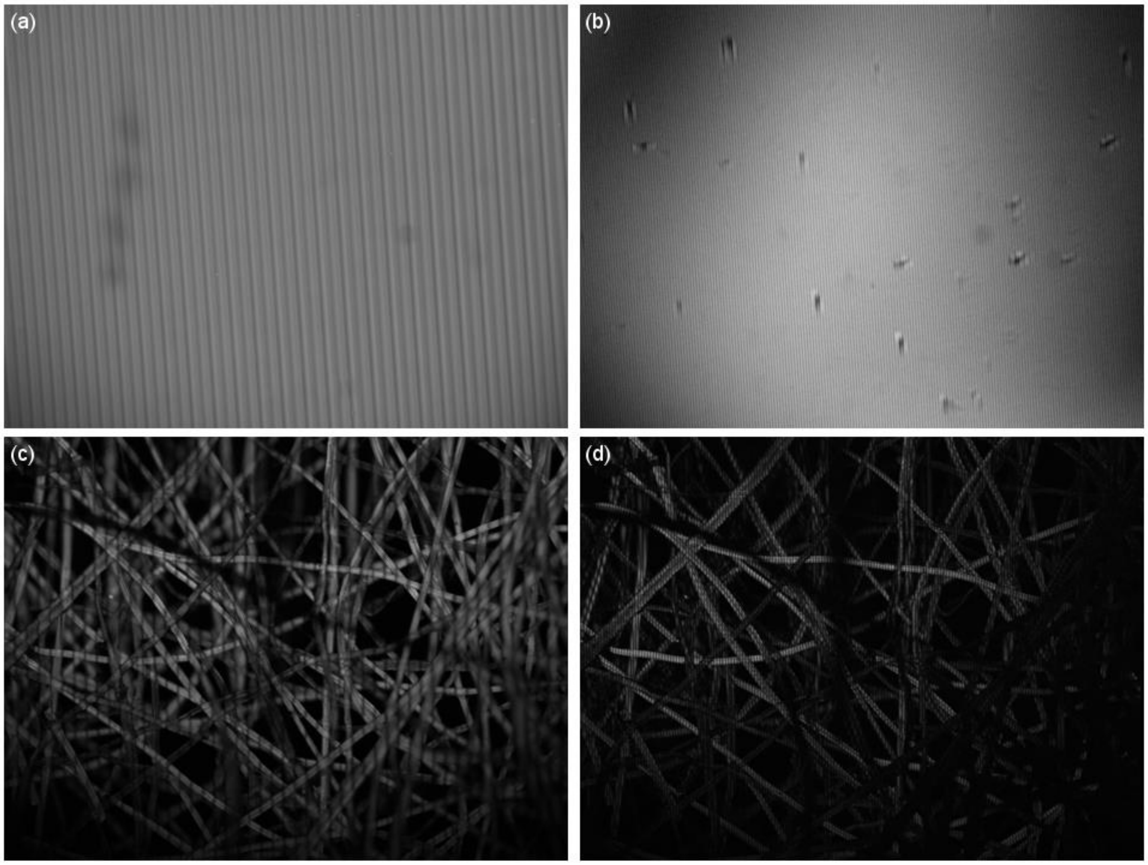

Fig. 3.11 (a) Residual grid pattern in a SI image of a plane mirror surface acquired with a 10 lp/mm grid. (b) Residual grid pattern in a SI image of a plane mirror surface acquired with a 40 lp/mm grid. (c) Residual grid pattern in a SI image of lens paper fibers labeled with fluorescent pen (10 lp/mm grid). (d) Residual grid pattern in a SI image of lens paper fibers labeled with fluorescent pen (40 lp/mm grid).

In order to minimize the appearance of the residual grid pattern artifact it is necessary to place the grid consistently and accurately. Furthermore, because the exposure time for a digital camera is often quite short (usually around 20 ms with bright fluorophores), it is the shifting of the grid pattern which represents the limiting factor in the overall speed of image collection.

The Zaber motorized translation stage used for grid shifting in this experimental work moves in discrete amounts known as microsteps. The number of steps required for each SI shift was initially calculated from the *step distance* specification provided by the manufacturer, and was then adjusted to minimize the appearance of the residual bar pattern. This number was determined to be 336 steps for the 10 lp/mm grid where a 33.3 μm shift is required to achieve a 2π/3 phase shift. This was often found to be sufficient for the simpler SIM program; however, in the continuous program, the residual bar pattern would appear and disappear in the SIM images, indicating that the actual shifted distance was not consistent even though the input (command) distance was constant.

To diagnose the problem, the grid and Zaber translation stage were moved in front of the HRME objective lens at the sample plane. The grid was mounted with its lines oriented in the vertical direction, backlit and brought into focus. The stage was translated through its entire range of lateral motion using a 336 step command increment (which should yield exactly 33.3 μm steps). The distance the grid actually moved was determined by extracting a horizontal intensity profile from the image and using the fact that the period of the pattern in the image is known to be 100 μm for the 10 lp/mm grid. Because both the grid pattern and direction of motion were one-dimensional, this method was sufficient for determining the shift distance and reduced the processing time (which is important due to the large number of images required to span the full range of the stage). Each one-dimensional profile was then cross-correlated with the previous profile (Fig. 3.12). The shift distance in pixels was determined by the peak in the cross-correlation function, and was then converted to linear distance (in this case, μm).

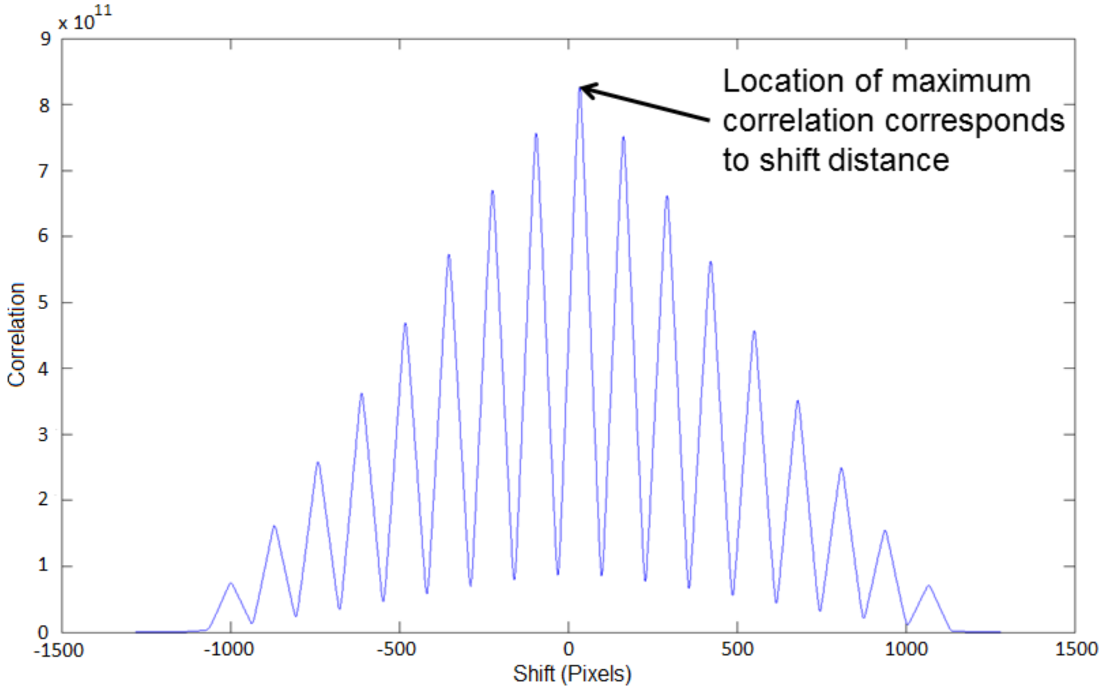

Fig. 3.12: Cross-correlation of two line profiles extracted from images acquired for consecutive shifts of the 10 lp/mm grid.

In Fig. 3.13 (a), the *measured* distance of each shift is plotted against the *reported* position of the stage, as determined by the stage's position sensor. The blue line shows the data when the stage was shifted in 336 step increments; for comparison the green line shows data for the stage shifted in 100 step increments. The data shows that the actual measured shift distance is not constant, even for a fixed command shift. It appears that the deviation from a constant shift is dependent on the absolute position of the stage in a periodic fashion and that this periodicity is the same for both 336 and 100 step command signals. This tendency is confirmed in Fig. 3.13 (b) which shows the actual shift distance divided by the number of steps, giving the actual shift per step commanded (detail Fig. 3.13 (c)). It is clear from the figure that the periodicity is the same in both data sets. This is not surprising because the stage uses a screw motor and this sort of deviation is common in screw motor actuators. In order to increase the consistency of the shift, a look-up-table (LUT) was created which applies the appropriate number of steps required to achieve the desired grid shift for any position of the motorized stage along its range of motion. This LUT was generated by first calculating the cross-correlation of the experimental 100 step/shift data with a series of pure sinusoids of increasing frequencies. All of the pure frequencies which resulted in a correlation coefficient greater than 0.05 were then summed together, normalizing each sinusoidal component by its corresponding correlation coefficient (whether this is theoretically the best way to model the behavior of the stage is not critical, provided it somewhat accurately reproduces the behavior of the stage; later a further “fixing” algorithm will be applied to the created LUT). The resulting sum of sinusoidal components was used to create a predicted step size for each position, shown in Fig. 3.13 (d). The predicted shift is shown in Fig. 3.13 (e) in red against the 336 step/shift (blue) and 100 step/shift (green) (detail Fig. 3.13 (f)). As can be seen, the data sets show good agreement.

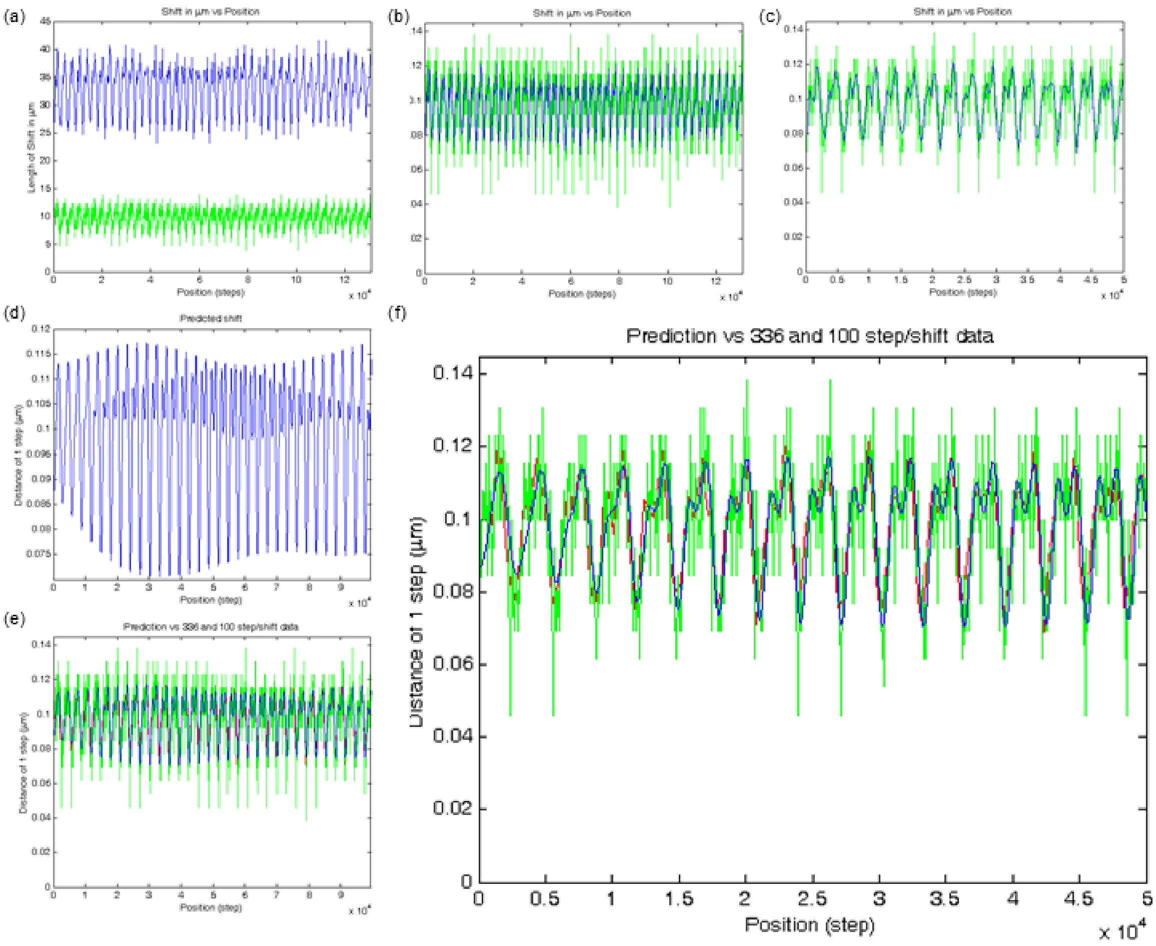

Fig. 3.13: (a) Measured shift distance for the translation stage for fixed command shifts, as a function of position along its range of motion. The blue line indicates a command shift of 336 steps, the green line indicates a command shift of 100 steps. (b) Measured shift distance per step for commands of 336 steps (blue) and 100 steps (green). (c) Expanded detail of panel (b). (d) Predicted step size as a function of position using an experimentally generated look-up table. (e) Predicted step size overlaid with measured step size for 336 step command shift (blue) and 100 step command shift (green). (f) Expanded detail of panel (e).

To quantify the improvement in shift accuracy provided by the LUT approach, Fig. 3.14 (a) shows a histogram of the deviation of the shift distance from ideal when a constant step number is used (this is the typical method used in SI microscopy). As can be seen, the range of deviation is quite large (approximately 30% of the shift distance) and with a standard deviation of greater than 10% of the ideal value (33.3 µm). In comparison, Fig. 3.14 (b) shows the same data when the look-up-table (LUT) method was used to determine the number of steps required to generate a 33.3 µm shift, rather than simply applying a constant command value. It is clear that the range of the deviation from the ideal shift has been greatly reduced (12-13% compared to 25-30%) and the standard deviation of the shift has been reduced from 4.25 to 1.5 µm. In order to further improve the performance of the LUT in achieving the expected lateral phase shift for SIM, an additional "fixing" algorithm was applied, working as follows. First, the stage is commanded to move to the end of its range of motion, i.e. the "zero position". The position is then queried from the stage and an image is collected. The stage then moves the appropriate number of steps, as read from the LUT. Then the position is queried again, an image collected, and the stage moves again. This is repeated as the stage moves through its full range of motion with an image collected at each position. The distances of the shifts are then computed as previously described. The deviation from the ideal shift is computed, this distance is divided by the average step size (as given by manufacturers specifications), to give the number of steps to add or remove from the LUT value, interpolating between positions. This was done several times; the results of 1, 2, 5, and 10 rounds of such "fixing" are shown in Fig. 3.14 (c)-(f). Unfortunately, this process was not found to significantly improve the positioning accuracy of the translation stage beyond that achieved by the LUT. This may be due to the fact that there are a large number of possible positions for the stage to be commanded to (over 130,000), considerably less than 1% of which are measured during the fixing algorithm (around 1 in 300 positions).

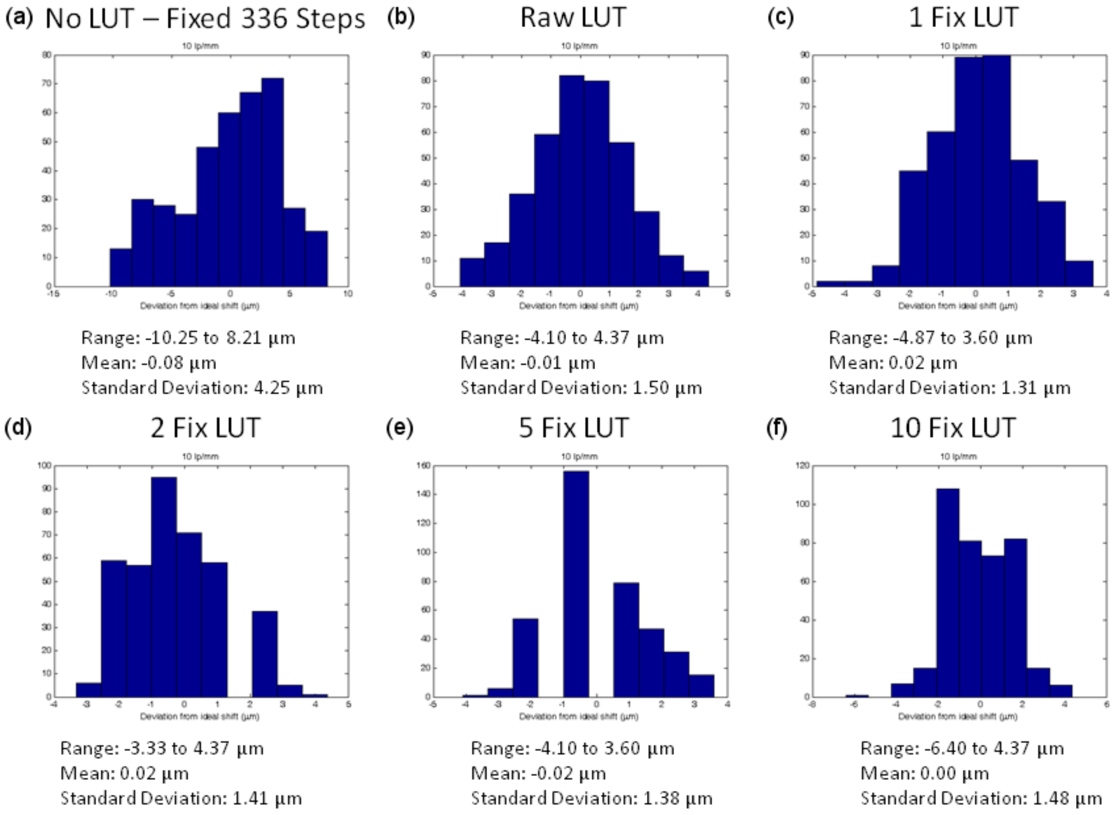

Fig. 3.14: (a) Shift distances using 336 step shift. (b) Shift distances using LUT. (c) Shift distances of LUT after 1 round of fixing algorithm. (d) Shift distances of LUT after 2 rounds of fixing algorithm. (e) Shift distances of LUT after 5 rounds of fixing algorithm. (f) Shift distances of LUT after 10 rounds of fixing algorithm.

Chapter 4: Summary & Conclusions

In this thesis, the imaging properties of the HRME imaging system were quantified for the first time. In the first section of Chapter 2, a simple geometric model was developed to predict the blur radius and intensity of labeled objects within the HRME image as a function of defocus. This model was then compared against experiments with fluorescently labeled beads in a phantom system, demonstrating good agreement between measured and expected values. The results of these experiments help to explain why proflavine has proven highly effective for imaging with the HRME system in pilot clinical studies. The fact that proflavine specifically labels nuclei and not the surrounding cytoplasm or organelles means that only the most superficial nuclei can be imaged effectively. Fluorescent emission from OOF nuclei rapidly loses intensity with defocus and fades to a low background which does not significantly decrease image contrast. As demonstrated, HRME produces images of comparable quality to confocal microendoscopy in proflavine stained tissue. If the imaging application requires the ability to assess nuclear morphology in terms of size, uniformity, crowding, etc., HRME with proflavine is an excellent imaging modality. However, if the application requires imaging any other cellular feature (e.g. immunostaining or fluorescein staining), HRME with proflavine will not provide images of the quality desired for diagnosis of pathology.

In order to expand the capability of HRME to image tissue stained with dyes other than proflavine, it is desirable to add the property of optical sectioning. Structured illumination (SI) is an imaging modality which exhibits this ability and is well suited for pairing with HRME because the hardware modifications are relatively minor and inexpensive in comparison to what would be required to implement laser-scanning confocal microendoscopy to achieve sectioning. By interposing a one-dimensional grid on a translation stage in the illumination path and synchronizing the image collection and grid translation, SI image collection can be achieved. As demonstrated in Chapter 3, SIM can be performed with or without an imaging fiber-bundle, removing OOF objects and generally improving image quality. The work in Chapter 3 outlined the theoretical underpinnings of SI and verified the performance of a custom built SI microscope against predicted behavior. Several strategies were suggested and examined for programming SI image collection, with the frame rate of each strategy quantified. Finally, the problem of the residual bar artifact which results from an inaccurate shift of the grid was addressed by developing a software-based method of reducing the appearance of the unwanted grid pattern.

While SI is an effective method of removing OOF signal from an image there are some considerations for its use in practice. All three images must be of the same FOV, with the same brightness, and there must be negligible sample motion within the FOV in order to effectively collect an image. When implemented with a grid on a translation stage, it is difficult to move the grid accurately enough to prevent the residual grid pattern from appearing in the final image and furthermore, the translation and settling time of the grid represents the rate limiting step for all but the longest exposure image collection. By using a spatial light modulator it may be possible to simultaneously address the challenge of grid shift accuracy and to increase the rate of image collection.

References

1. Wang KK, Sampliner RE. Diagnosis, surveillance and therapy of Barrett's esophagus. Am J Gastroenterol. 2008;103:788-97.

2. Goetz M, Kiesslich R. Advances of endomicroscopy for gastrointestinal physiology and diseases. American Journal of Physiology-Gastrointestinal and Liver Physiology. 2010;298(6):G797-806.

3. Polglase AL, McLaren WJ, Skinner SA, Kiesslich R, Neurath MF, Delaney PM. A fluorescence confocal endomicroscope for in vivo microscopy of the upper-and the lower-GI tract. Gastrointest Endosc. 2005;62(5):686-95.

4. Thong PS, Olivo M, Kho K, Zheng W, Mancer K, Harris M, et al. Laser confocal endomicroscopy as a novel technique for fluorescence diagnostic imaging of the oral cavity. J Biomed Opt. 2007;12(1):014007,014007-8.

5. Astner S, Dietterle S, Otberg N, Röwert-Huber H, Stockfleth E, Lademann J. Clinical applicability of in vivo fluorescence confocal microscopy for noninvasive diagnosis and therapeutic monitoring of nonmelanoma skin cancer. J Biomed Opt. 2008;13(1):014003,014003-12.

6. Tan J, Quinn M, Pyman J, Delaney P, McLaren W. Detection of cervical intraepithelial neoplasia in vivo using confocal endomicroscopy. BJOG: An International Journal of Obstetrics & Gynaecology. 2009;116(12):1663-70.

7. Dunbar KB, Okolo III P, Montgomery E, Canto MI. Confocal laser endomicroscopy in barrett's esophagus and endoscopically inapparent barrett's neoplasia: A prospective, randomized, double-blind, controlled, crossover trial. Gastrointest Endosc. 2009;70(4):645-54.

8. Wallace MB, Sharma P, Lightdale C, Wolfsen H, Coron E, Buchner A, et al. Preliminary accuracy and interobserver agreement for the detection of intraepithelial neoplasia in barrett's esophagus with probe-based confocal laser endomicroscopy. Gastrointest Endosc. 2010;72(1):19-24.

9. Lane PM, Lam S, McWilliams A, Anderson MW, MacAulay CE. Confocal fluorescence microendoscopy of bronchial epithelium. J Biomed Opt. 2009;14(2):024008,024008-10.

10. Tanbakuchi AA, Udovich JA, Rouse AR, Hatch KD, Gmitro AF. In vivo imaging of ovarian tissue using a novel confocal microlaparoscope. Obstet Gynecol. 2010;202(1):90. e1,90. e9.

11. Rouse AR. Multi-spectral confocal microendoscope for in-vivo imaging. . 2004.

12. Webb RH. Confocal optical microscopy. Reports on Progress in Physics. 1996;59(3):427.

13. Wilson T, Carlini A. Size of the detector in confocal imaging systems. Opt Lett. 1987;12(4):227-9.

14. Gmitro AF, Aziz D. Confocal microscopy through a fiber-optic imaging bundle. Opt Lett. 1993;18(8):565-7.

15. Sabharwal YS, Rouse AR, Donaldson L, Hopkins MF, Gmitro AF. Slit-scanning confocal microendoscope for high-resolution< i> in Vivo</i> imaging. Appl Opt. 1999;38(34):7133-44.

16. Knittel J, Schnieder L, Buess G, Messerschmidt B, Possner T. Endoscope-compatible confocal microscope using a gradient index-lens system. Opt Commun. 2001;188(5):267-73.

17. Juškattis R, Wilson T, Watson T. Real-time white light reflection confocal microscopy using a fibre-optic bundle. Scanning. 1997;19(1):15-9.

18. Dromard T, Ravaine V, Ravaine S, Lévêque J, Sojic N. Remote in vivo imaging of human skin corneocytes by means of an optical fiber bundle. Rev Sci Instrum. 2007;78(5):053709,053709-6.

19. Muldoon TJ, Pierce MC, Nida DL, Williams MD, Gillenwater A, Richards-Kortum R. Subcellular-resolution molecular imaging within living tissue by fiber microendoscopy. Optics express. 2007;15(25):16413.

20. Muldoon TJ, Anandasabapathy S, Maru D, Richards-Kortum R. High-resolution imaging in barrett's esophagus: A novel, low-cost endoscopic microscope. Gastrointest Endosc. 2008;68(4):737-44.

21. Zhong W, Celli J, Rizvi I, Mai Z, Spring B, Yun S, et al. In vivo high-resolution fluorescence microendoscopy for ovarian cancer detection and treatment monitoring. Br J Cancer. 2009;101(12):2015-22.

22. Rosbach KJ, Shin D, Muldoon TJ, Quraishi MA, Middleton LP, Hunt KK, et al. High-resolution fiber optic microscopy with fluorescent contrast enhancement for the identification of axillary lymph node metastases in breast cancer: A pilot study. Biomed.Opt.Express. 2010;1(3):911-22.

23. Muldoon TJ, Roblyer D, Williams MD, Stepanek VM, Richards–Kortum R, Gillenwater AM. Noninvasive imaging of oral neoplasia with a high-resolution fiber-optic microendoscope. Head Neck. 2012;34(3):305-12.

24. Elahi SF, Miller SJ, Joshi B, Wang TD. Targeted imaging of colorectal dysplasia in living mice with fluorescence microendoscopy. Biomedical optics express. 2011;2(4):981-6.

25. Pierce M, Yu D, Richards-Kortum R. High-resolution fiber-optic microendoscopy for in situ cellular imaging. Journal of visualized experiments: JoVE. 2011(47).

26. Mufti N, Kong Y, Cirillo JD, Maitland KC. Fiber optic microendoscopy for preclinical study of bacterial infection dynamics. Biomedical optics express. 2011;2(5):1121.

27. Regunathan R, Woo J, Pierce MC, Polydorides AD, Raoufi M, Roayaie S, et al. Feasibility and preliminary accuracy of high-resolution imaging of the liver and pancreas using FNA compatible microendoscopy (with video). Gastrointest Endosc. 2012;76(2):293-300.

28. Vila PM, Park CW, Goldstein GH, Levy L, Gurudutt VV, Teng MS, et al. Discrimination of benign and neoplastic mucosa with a high-resolution microendoscope (HRME) in head and neck cancer. Annals of surgical oncology. 2012;19(11):3534-9.

29. Göbel W, Brucker D, Kienast Y, Johansson A, Kniebühler G, Rühm A, et al. Optical needle endoscope for safe and precise stereotactically guided biopsy sampling in neurosurgery. Opt.Express. 2012;20(24):26117-26.

30. Shao P, Shi W, Hajireza P, Zemp RJ. Integrated micro-endoscopy system for simultaneous fluorescence and optical-resolution photoacoustic imaging. J Biomed Opt. 2012;17(7):0760241-4.

31. Wall RA, Barton JK. Fluorescence-based surface magnifying chromoendoscopy and optical coherence tomography endoscope. J Biomed Opt. 2012;17(8):0860031-7.

32. Pierce MC, Vila PM, Polydorides AD, Richards-Kortum R, Anandasabapathy S. Low-cost endomicroscopy in the esophagus and colon. Am J Gastroenterol. 2011;106(9):1722.

33. Pierce MC, Schwarz RA, Bhattar VS, Mondrik S, Williams MD, Lee JJ, et al. Accuracy of in vivo multimodal optical imaging for detection of oral neoplasia. Cancer Prevention Research. 2012;5(6):801-9.

34. Quinn MK, Bubi TC, Pierce MC, Kayembe MK, Ramogola-Masire D, Richards-Kortum R. High-resolution microendoscopy for the detection of cervical neoplasia in low-resource settings. PLoS One. 2012;7(9):e44924.

35. Pierce MC, Guan Y, Quinn MK, Zhang X, Zhang W, Qiao Y, et al. A pilot study of low-cost, high-resolution microendoscopy as a tool for identifying women with cervical precancer. Cancer Prevention Research. 2012;5(11):1273-9.

36. Subbarao M, Surya G. Depth from defocus: A spatial domain approach. International Journal of Computer Vision. 1994;13(3):271-94.

37. Chaudhari AJ, Darvas F, Bading JR, Moats RA, Conti PS, Smith DJ, et al. Hyperspectral and multispectral bioluminescence optical tomography for small animal imaging. Phys Med Biol. 2005;50(23):5421.

38. Garofalakis A, Zacharakis G, Filippidis G, Sanidas E, Tsiftsis DD, Ntziachristos V, et al. Characterization of the reduced scattering coefficient for optically thin samples: Theory and experiments. Journal of Optics A: Pure and Applied Optics. 2004;6(7):725.

39. Cubeddu R, Pifferi A, Taroni P, Torricelli A, Valentini G. A solid tissue phantom for photon migration studies. Phys Med Biol. 1997;42(10):1971.

40. Cuccia DJ, Bevilacqua F, Durkin AJ, Ayers FR, Tromberg BJ. Quantitation and mapping of tissue optical properties using modulated imaging. J Biomed Opt. 2009;14(2):024012,024012-13.

41. El Hallani S, Poh C, Macaulay C, Follen M, Guillaud M, Lane P. Ex vivo confocal imaging with contrast agents for the detection of oral potentially malignant lesions. Oral Oncol. 2013.

42. Neil M, Juskaitis R, Wilson T. Method of obtaining optical sectioning by using structured light in a conventional microscope. Opt Lett. 1997;22(24):1905-7.

43. Chasles F, Dubertret B, Boccara AC. Optimization and characterization of a structured illumination microscope. Optics Express. 2007;15(24):16130-40.

44. Karadaglić D, Juškaitis R, Wilson T. Confocal endoscopy via structured illumination. Scanning. 2002;24(6):301-4.

45. Bozinovic N, Ventalon C, Ford T, Mertz J. Fluorescence endomicroscopy with structured illumination. Opt.Express. 2008;16(11):8016-25.

46. Gustafsson MG, Agard DA, Sedat JW. Doubling the lateral resolution of wide-field fluorescence microscopy using structured illumination. BiOS 2000 the international symposium on biomedical optics; International Society for Optics and Photonics; 2000.

47. Gustafsson MG. Surpassing the lateral resolution limit by a factor of two using structured illumination microscopy. J Microsc. 2000;198(2):82-7.

48. Gustafsson MG. Nonlinear structured-illumination microscopy: Wide-field fluorescence imaging with theoretically unlimited resolution. Proc Natl Acad Sci U S A. 2005;102(37):13081-6.

49. Gustafsson MG, Shao L, Carlton PM, Wang CR, Golubovskaya IN, Cande WZ, et al. Three-dimensional resolution doubling in wide-field fluorescence microscopy by structured illumination. Biophys J. 2008;94(12):4957.

50. Hirvonen LM, Wicker K, Mandula O, Heintzmann R. Structured illumination microscopy of a living cell. European Biophysics Journal. 2009;38(6):807-12.

51. Zhang H, Zhao M, Peng L. Nonlinear structured illumination microscopy by surface plasmon enhanced stimulated emission depletion. Optics Express. 2011;19(24):24783-94.

52. Rego EH, Shao L, Macklin JJ, Winoto L, Johansson GA, Kamps-Hughes N, et al. Nonlinear structured-illumination microscopy with a photoswitchable protein reveals cellular structures at 50-nm resolution. Proceedings of the National Academy of Sciences. 2012;109(3):E135-43.

53. Stokseth PA. Properties of a defocused optical system. JOSA. 1969;59(10):1314-21.